Chemical Science

EDGE ARTICLE

View Article Online
View Journal | View Issue

Cite this: *Chem. Sci.*, 2014, **5**, 4661

Full-dimensional potentials and state couplings and multidimensional tunneling calculations for the photodissociation of phenol†

Ke R. Yang, Xuefei Xu, Jingjing Zheng and Donald G. Truhlar*

Received 2nd July 2014
Accepted 6th August 2014

DOI: 10.1039/c4sc01967a

www.rsc.org/chemicalscience

We present an improved version of the anchor points reactive potential (APRP) method for potential energy surfaces; the improvement for the surfaces themselves consists of using a set of internal coordinates with better global behavior, and we also extend the method to fit the surface couplings. We use the new method to produce a 3 × 3 matrix of diabatic potential energy surfaces and couplings for the photodissociation of phenol as functions of 33 nonredundant internal coordinates. The diabatic potential matrix is based on two kinds of calculations at a sequence of anchor points along the O–H dissociation coordinate: (1) fourfold way diabatic calculations based on MC-QDPT/jul-cc-pVDZ calculations for the potential energy surfaces and diabatic couplings as functions of the O–H bond stretch, C–O–H bond angle, and C–C–O–H torsion and for the diabatic couplings as functions of the nine out-of-plane phenoxyl distortion coordinates and (2) M06-2X/jul-cc-pVDZ density functional Hessian calculations for the potentials along the 30 vibrational coordinates of the phenoxyl group. The potential energy surfaces and couplings are used to calculate and characterize adiabatic surfaces and conical intersections, and the resulting equilibrium geometries, vibrational frequencies, and vertical excitation energies are in good agreement with available reference data. We also calculate the geometries of the minimum energy conical intersections. The surfaces and couplings are used for full-dimensional tunneling calculations of the adiabatic photodissociation rate, *i.e.*, the rate of O–H bond fission following photoexcitation. Finally we use the couplings to provide indicators of which vibrational modes are effective in promoting dissociation.

1. Introduction

By separating the electronic and nuclear degrees of freedom, the widely used Born–Oppenheimer (BO) approximation[1] leads the useful concepts of adiabatic states and potential energy surfaces (PESs). Adiabatic PESs are $(3N - 6)$-dimensional hypersurfaces (where N is the number of atoms in a molecule) with $(3N - 8)$-dimensional cuspidal ridges along conical intersection (CI) seams where two or more adiabatic PESs are degenerate. The couplings between nuclear motions and electronic motions are usually called nonadiabatic couplings, and they are responsible for nonadiabatic transitions between different adiabatic states and for the development of coherent superpositions of adiabatic electronic states as the nuclear positions evolve. Nonadiabatic couplings are usually small in regions removed from conical intersection seams and from the regions of near degeneracy surrounding them, and when they are small, nuclear motions can be treated to a good approximation as evolving on a single adiabatic PES.[2]

The BO approximation breaks down when two or more adiabatic PESs approach closely or intersect. The nonadiabatic couplings vary rapidly in such regions and become singular at CIs, thereby promoting nonadiabatic transitions in those regions. To model electronically nonadiabatic processes where two or more electronic states are coupled *via* nonadiabatic couplings, one can use either the adiabatic representation or a diabatic representation.[3] In the adiabatic representation, which is unique, the electronic Hamiltonian (always defined here, as usual, to also include nuclear repulsion) is diagonal; the diagonal elements are the adiabatic PESs V_i, and the semiclassically dominant nonadiabatic couplings are vectors deriving from the action of nuclear momentum operators on the adiabatic electronic wave functions. In a diabatic representation, these vector couplings are negligible (or assumed negligible), and diabatic electronic states and their associated PESs, U_{ii}, are coupled through scalar off-diagonal elements, U_{ij}, of the electronic Hamiltonian; these off-diagonal elements are called diabatic couplings. Diabatic states are sometimes called quasidiabatic states because strict diabatic states, in which the nuclear-momentum couplings are not just negligible but zero, do not exist in general.[4] Thus diabatic states are not uniquely defined,

Department of Chemistry, Chemical Theory Center, Supercomputing Institute, University of Minnesota, Minneapolis, Minnesota 55455-0431, USA. E-mail: truhlar@umn.edu

† Electronic supplementary information (ESI) available. See DOI: 10.1039/c4sc01967a

and many schemes have been proposed to construct diabatic states.[5–31]

Potential energy surfaces can be constructed in either the adiabatic or diabatic representation, but the cuspidal ridges of the adiabatic potentials and the singularity of nonadiabatic couplings in ubiquitous conical intersection regions[32] prevent the analytic representation of adiabatic PESs and nonadiabatic couplings. On the other hand, diabatic potentials and couplings change smoothly with respective to geometrical variations, and they allow for convenient representation. After one has the diabatic PESs available, one can carry out dynamics calculations in either the diabatic or the adiabatic representation, where the latter would be obtained from the diabatic PESs and diabatic couplings by transformations. In the present article, we develop an analytic representation of the multidimensional coupled potential energy surfaces for phenol in the diabatic representation, in particular we use potentials obtained by fourfold-way diabatization,[17,31,33] and the resulting diabatic surfaces and couplings yield the adiabatic surfaces and couplings by standard equations given elsewhere.[34]

As a prototypical process in photochemistry, the photodissociation of phenol to phenoxyl radical and H atom has been studied extensively both experimentally and theoretically, especially in recent years.[33,35–57] The photodissociation of phenol involves passage through a crossing region of the $^1\pi\pi^*$ excited state and the $^1\pi\sigma^*$ state, which is repulsive along the O–H dissociation coordinate r, and this crossing region surrounds a conical intersection (CI1) of the $^1\pi\pi^*$ and $^1\pi\sigma^*$ states. The repulsive $^1\pi\sigma^*$ state further crosses the $^1\pi\pi$ ground state at another conical intersection (CI2) at larger r. Thus we need to consider three adiabatic PESs called V_i, with $i = 1, 2, 3$, or three diabatic PESs; the latter are the diagonal elements U_{ii} of a 3×3 matrix potential, but we call them U_i for simplicity. The roles of the two CIs in the photodissociation of phenol and of the vibrational modes that affect the probabilities of transitions at the CIs have been studied extensively, leading to stimulating insights and debates. Wave-packet studies[37,43,50,51] have been carried out to study the dynamics of phenol photodissociation, but they were performed with two-dimensional potential energy surfaces by considering only the O–H stretching coordinate and a selected coupling mode. Due to the complexity of the phenol molecule, which has 13 atoms and whose PESs are therefore 33-dimensional, only recently was there an attempt to get higher-dimensional PESs.[54] Very recently, Zhu and Yarkony constructed full-dimensional coupled PESs of phenol using a diabatic Hamiltonian whose domain of definition was constructed using quasiclassical surface hopping trajectories.[55] In the present article we present full-dimensional coupled PESs of phenol as obtained by a quite different approach. Either set of coupled PESs should be able to lead to more complete studies of the phenol photodissociation process including the key role of the phenoxyl ring vibrations.

The size of phenol prevents the use of many PES fitting approaches, such as permutation-invariant polynomials,[58–60] and the interpolated moving-least squares[61–63] method, that have been widely used for smaller systems. Here we use an improved version of our recently proposed anchor points reactive potential (APRP) method,[64] which combines general analytic forms for large-amplitude modes with molecule-specific and anchor-point-specific molecular mechanics terms for small-amplitude modes, to obtain full-dimensional semi-global diabatic PESs for photodissociation of phenol. The improvement consists in the use of internal coordinates with better global behavior. The surfaces are based on partitioning the internal coordinates into three groups: the reaction coordinate r (also called the primary coordinate), secondary coordinates **s**, and tertiary coordinates **Q**, and the potentials are semiglobal in that they are defined for all possible values of the primary and secondary coordinates but only for small-amplitude vibrations of the tertiary coordinates away from the planar reference geometry of the phenoxyl fragment.

The geometry and atomic numbering of phenol and phenoxyl radical are shown in Fig. 1. (The structures mentioned in the caption of Fig. 1 will be explained more fully below.) In the present work, the O–H fission coordinate was chosen as the reaction coordinate r; the C1–O–H bond angle θ and C2–C1–O–H torsion angle ϕ were chosen as secondary coordinates; and the internal coordinates of phenoxyl were chosen as tertiary coordinates **Q**. We use smooth diabatic potentials and couplings along r and ϕ calculated previously[33] combined with new calculations of the diabatic potentials and couplings along θ and small-amplitude-vibration approximations of the dependence of the potentials on the tertiary coordinates at several anchor points (explained below).

Upon dissociation, the ground $^1\pi\pi$ state of phenol diabatically connects to the excited $\tilde{A}\ ^2B_2$ state of phenoxyl radical and H atom, while the repulsive $^1\pi\sigma^*$ state diabatically connects to the ground $\tilde{X}\ ^2B_1$ state of phenoxyl radical and H atom. These diabatic connections are apparent in Fig. 2, which more properly belongs in the results section but is placed here to provide the reader with a picture of the general shapes of the potential surfaces to make the presentation in Section 2 clearer.

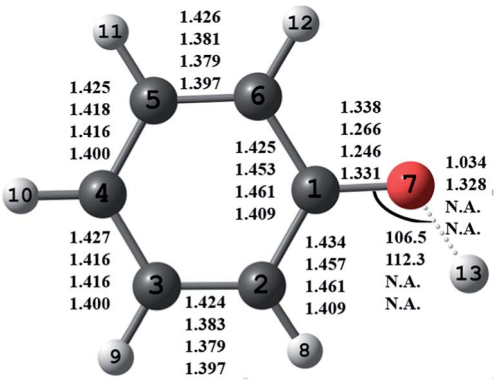

Fig. 1 The figure shows the structure of the transition state on adiabatic surface S_1, and it also shows four sets of geometrical parameters for key eight C–C, C–O, and O–H bond lengths (in Å) and the C–O–H bond angle (in degrees). From top to bottom are values for the equilibrium geometry of the S_1 state of phenol, the saddle point of the S_1 state (the structure shown), the $\tilde{X}\ ^2B_1$ state of phenoxyl radical, and the $\tilde{A}\ ^2B_2$ state phenoxyl radical. "N.A." denotes not applicable.

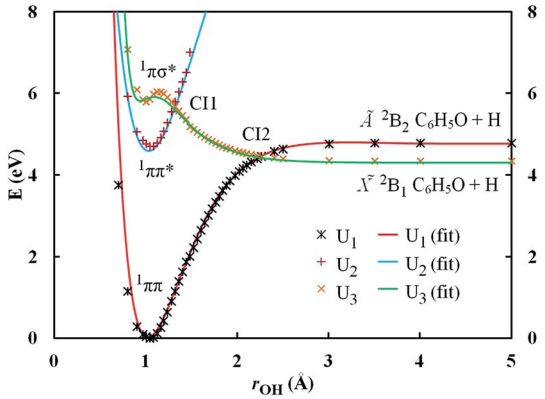

Fig. 2 Calculated and APRP diabatic potential energy curves of phenol along the O–H dissociation coordinate. The other geometric parameters are fixed at their values at the equilibrium geometry of ground state phenol. The locations of the conical intersections on the APRP surfaces for these cuts are $r = 1.316$ Å and $r = 2.231$ Å, respectively.

This paper has two "take home" messages – (i) improved methodology that others may want to adopt and (ii) new insights into the excited state photochemistry of a prototype molecule. Because the paper is multi-faceted, we close the introduction with a guide to the contents of the various sections.

Section 2 presents the improved version of the APRP method. The APRP method stands in relation to full surface fitting as combined quantum mechanical and molecular mechanical (QM/MM) methods stand in relation to pure quantum mechanics.[65] In QM/MM methods, most of a system is treated by MM, but a subset of atoms is treated by QM. In APRP, the dependence of the potential on most coordinates (called tertiary coordinates) is treated by MM, but the dependence on a subset of the coordinates (called primary and secondary coordinates) is treated by completely general surface fitting. Furthermore, the treatment of the MM subsystem in the APRP goes beyond conventional MM in several respects: first, although the dependence of the potential on tertiary coordinates uses a type of MM functional form, the coordinates are chosen to have better global behavior than those usually used in MM; second, the parameters in the MM part are not general parameters chosen to be reasonable for typical systems, but rather than are system specific; third, as compared to previous system-specific MM methods,[66,67] the MM parameters vary as functions of the primary coordinates. A key element of the treatment is that, unlike conventional MM, the APRP method is applicable to reactive systems.

Section 2 contains many equations; although these are the heart of the paper, readers only interested in take home message (ii) need not fully absorb these equations in order to read the later sections. Section 3 presents the results of applying the APRP method not just to the ground-state potential energy surface of phenol but to a 3 × 3 matrix representation that yields the three lowest singlet states and their couplings. We use the results of this fit to understand the stationary points on the adiabatic surfaces, the multidimensional character of electronically adiabatic tunneling, the relation between the thickness of a barrier and its closeness to a conical intersection, the conical intersection seams both for geometries where the diabatic coupling vanishes by symmetry and for general geometries where there is no symmetry (C_1 point group), and the possible role of various normal-mode vibrations in the photodissociation process.

2. Methods and computational details

2.1. Anchor points reactive potential (APRP) method for diabatic potentials

Here we summarize the APRP method, specializing the description to the case of phenol photodissociation. The potential of diabatic state i is written as

$$U_i = U_i^{[1]}(r) + U_i^{[2]}(\mathbf{s}|r) + U_i^{[3]}(\mathbf{Q}|r), \tag{1a}$$

where $f(x|r)$ denotes a function with a dependence on x and a parametric dependence on r, and the three terms on the right side are called the primary, secondary, and tertiary terms. General functional forms were used to fit $U_i^{[1]}$ and $U_i^{[2]}$ with tertiary coordinates fixed at the reference geometry, and we take $U_i^{[2]}$ to be separable:

$$U_i^{[2]} = U_i^{[2,\phi]}(\phi|r) + U_i^{[2,\theta]}(\theta|r). \tag{1b}$$

The tertiary potentials are described by interpolation between preselected anchor points with tent functions:

$$U_i^{[3]} = \sum_{a=1}^{N_A} U_i^{[a]}\left(\mathbf{Q}^{[a]}\right) T_i^{[a]}(r), \tag{2}$$

where $U_i^{[a]}(\mathbf{Q}^{[a]})$ is the expansion of the potential energy of diabatic state i around anchor point a, and $T_i^{[a]}(r)$ is the tent function at anchor point a.

The tent functions are defined by

$$T_i^{[1]} = \begin{cases} 1 & r < r_i^{[1]} \\ \dfrac{\left(r - r_i^{[2]}\right)^4}{\left(r - r_i^{[2]}\right)^4 + \left(r - r_i^{[1]}\right)^4} & r_i^{[1]} \le r < r_i^{[2]} \end{cases}, \tag{3a}$$

$$T_i^{[a]} = \begin{cases} \dfrac{\left(r - r_i^{[a-1]}\right)^4}{\left(r - r_i^{[a]}\right)^4 + \left(r - r_i^{[a-1]}\right)^4} & r_i^{[a-1]} \le r < r_i^{[a]} \\ & \text{for } a = 2, \ldots, N_A - 1, \\ \dfrac{\left(r - r_i^{[a+1]}\right)^4}{\left(r - r_i^{[a+1]}\right)^4 + \left(r - r_i^{[a]}\right)^4} & r_i^{[a]} \le r < r_i^{[a+1]} \end{cases} \tag{3b}$$

$$T_i^{[N_A]} = \begin{cases} \dfrac{\left(r - r_i^{[N_A-1]}\right)^4}{\left(r - r_i^{[N_A]}\right)^4 + \left(r - r_i^{[N_A-1]}\right)^4} & r_i^{[N_A-1]} \le r < r_i^{[N_A]} \\ 1 & r_i^{[N_A]} \le r \end{cases}. \tag{3c}$$

In the present case of phenol, all diabatic calculations were carried out by fourfold-way diabatization using multi-configurational quasi-degenerate perturbation theory (MC-QDPT)[68] with the jul-cc-pVDZ basis set,[69] as described previously.[33] More specifically, we calculated the diabatic states U_1 ($^1\pi\pi$), U_2 ($^1\pi\pi^*$), and U_3 ($^1\pi\sigma^*$) along the chosen reaction coordinate r (O–H distance) and secondary coordinates θ (C1–O–H bond angle) and ϕ (C2–C1–O–H torsion) with other coordinates fixed, and we used these calculations to fit the primary and secondary potentials. The scans of r and ϕ were performed in the same way as in the previous work;[33] in particular, rigid scans of the C1–O–H bend (θ, with values of 90, 100, 107, 120, and 130°) were carried out at various r from 0.964 to 5.0 Å with other coordinates taken as the same as those obtained for the planar equilibrium geometry of ground-state phenol by the complete-active-space self-consistent-field (CASSCF)[70] method with the aug-cc-pVTZ basis set.[71]

Primary potentials. The primary potential of the diabatic $^1\pi\pi$ state was fit to the Varshni model potential,[72] given by.

$$U_1^{[1]} = D_1\{1 - (r_1/r)\exp[-\beta_1((r_1/r)^2 - 1)]\}^2. \quad (4)$$

The diabatic $^1\pi\pi^*$ state has a minimum near the ground-state equilibrium distance r_e, and it crosses the diabatic first $^1\pi\sigma^*$ state at about 1.3 Å and a second $^1\pi\sigma^*$ state of higher energy at about 1.5 Å. For the photodissociation of phenol, the $^1\pi\pi^*$ state is only important in the small-r range, so it is acceptable to fit the $U_2^{[1]}(r)$ curve to a Morse potential[73] and we used

$$U_2^{[1]} = D_2\{1 - \exp[-\alpha(r - r_2)]\}^2 + A_2. \quad (5)$$

A three-term function was used to fit the repulsive potential of first diabatic $^1\pi\sigma^*$ state:

$$U_3^{[1]} = \sum_{i=1}^{3} a_i \exp[-\alpha_{3,i}(r - r_{3,i})] + A_3. \quad (6)$$

Secondary potentials. The torsion potential $U_i^{[2]}(\phi|r)$ of diabatic state i is fitted with the following expression:

$$U_i^{[2,\phi]} = \sum_{j=1}^{n_j} W_{i,j}(r)(1 - \cos 2\phi)^j, \quad (7)$$

where n_j is the number of terms to expand the torsion potential [$n_j = 1$ for diabatic states U_1 and U_2 ($^1\pi\pi$ and $^1\pi\pi^*$) and $n_j = 2$ for diabatic state U_3 ($^1\pi\sigma^*$)], and $W_{i,j}$ is the barrier height of the jth term. The latter was expanded as a linear combination of Gaussian functions, given by

$$W_{i,j} = \sum_{k=1}^{n_k} A_{i,j,k} \exp\left[-\alpha_{i,j,k}\left(r - r_{i,j,k}\right)^2\right]. \quad (8)$$

In fitting the C1–O–H bending potentials, we used $\cos\theta$ rather than θ in order to have the proper symmetry of bend potentials with respect to $\pi - \Delta\theta$ and $\pi + \Delta\theta$:

$$U_i^{[2,\theta]} = \sum_{j=2}^{n_j} k_{i,j}(r)(\cos\theta - \cos\theta_{i,0}(r))^j \quad (9)$$

The force constant $k_{i,j}$ was further expanded with linear combinations of Gaussians similar to eqn (8). A hyperbolic tangent function is used to fit the dependence of $\cos\theta_{i,0}$ on r:

$$\cos\theta_{i,0} = \cos\theta_{i,1} + \frac{1 + \tanh(a_{i,1}(r - r_{i,1}))}{2}(\cos\theta_{i,2} - \cos\theta_{i,1}) \quad (10)$$

where $\cos\theta_{i,1}$ and $\cos\theta_{i,2}$ are constant parameters.

Tertiary potentials. Now we turn to $U_i^{[3]}$, which depends on tertiary coordinates and depends parametrically on r through the use of anchor points. The dependence of the diabatic potentials on tertiary coordinates is needed only for small extensions from planar geometries. For planar geometries, the diabatic states U_1 ($^1\pi\pi$), U_2 ($^1\pi\pi^*$), and U_3 ($^1\pi\sigma^*$) belong to the A', A', and A''irreducible representations, respectively, and as shown in Fig. 2, the two states with same symmetries are always well separated, while the intersecting diabatic states along the reaction coordinate r have different symmetries; thus the adiabatic states are good approximations to the diabatic states under the C_s symmetry constraint of the planar geometries. Hence we chose anchor points with planar structures and obtained the diabatic states at each anchor point by adiabatic calculations of the correct symmetry as described next.

For diabatic states U_1 ($^1\pi\pi$) and U_3 ($^1\pi\sigma^*$), since they are the lowest states of their symmetry, we utilize ground-state Kohn–Sham calculations with the M06-2X exchange-correlation potential[74] and the jul-cc-pVDZ basis set to perform partial optimization (optimizing all secondary and tertiary coordinates for fixed r) and calculate the Hessians at each of the anchor points. For diabatic state U_2 ($^1\pi\pi^*$), since it is an excited state (S_1) in A' symmetry, time-dependent density functional theory (TDDFT)[75,76] was used to perform the partial optimization and Hessian calculations, again with the M06-2X exchange-correlation potential and the jul-cc-pVDZ basis set.

For each diabatic state, four planar anchor points were chosen along the O–H dissociation coordinate; for U_1, they are at $r = 0.964$, 1.32, 2.00, and 5.00 Å, and for U_2 and U_3, they are at $r = 0.964$, 1.32, 2.26, and 5.00 Å. The first anchor point for each of the diabatic states has the ground-state equilibrium O–H bond length calculated by CASSCF/jul-cc-pVDZ; the second anchor point was chosen to have an O–H bond length close to the first conical intersection (CI1) in planar geometry; the third anchor points were chosen to have an O–H bond length close to the second conical intersection (CI2); and the final anchor points were chosen to yield the correct asymptotic limit of phenoxyl radical.

The ground state of phenoxyl is $\tilde{X}\ ^2B_1$ and it has a low-lying $\tilde{A}\ ^2B_2$ excited state; these states connect diabatically to surfaces U_3 ($^1\pi\sigma^*$) and U_1 ($^1\pi\pi$), respectively, and they were optimized with UM06-2X/jul-cc-pVDZ. The geometric parameters and Hessians of phenoxyl in these two states were used for the final anchor points with $r = 5.00$ Å. For anchor points with other O–H bond lengths, geometrical parameters and Hessians were obtained with partial optimizations. Since U_2 state is not very relevant after the first conical intersection (CI1), the geometrical parameters and Hessian elements at $r = 1.32$ Å were used for it at the next two anchor points $r = 2.26$ Å and 5.00 Å.

In our original APRP, the tertiary potential around anchor point a was expanded as

$$U_i^{[a]} = U_{\mathrm{rel},i}^{[a]} + \frac{1}{2}\mathbf{Q}_i^{[a]^{\mathrm{T}}}\,\mathbf{F}_i^{[a]}\mathbf{Q}_i^{[a]}, \tag{11}$$

where $U_{\mathrm{rel},i}^{[a]}$ is the energy of state i at the partially optimized geometry of anchor point a, relative to the energy of a fixed reference geometry, $\mathbf{F}_i^{[a]}$ is the partial force constant matrix, and $\mathbf{Q}_i^{[a]}$ is a column vector of the internal displacements around anchor structure a with elements

$$Q_{ji}^{[a]} = Q_j - Q_{\mathrm{e},ji}^{[a]}, \tag{12}$$

where Q_j is an internal coordinate, and $Q_{\mathrm{e},ji}^{[a]}$ is the optimized value of Q_j for state i in the constrained optimized geometry of anchor point a. By partitioning internal displacements $\mathbf{Q}_i^{[a]}$ into stretches (S), bends (B), and torsions (T), eqn (11) can be written as

$$U_i^{[a]} = U_{\mathrm{rel},i}^{[a]} + U_i^{\mathrm{SS},a} + U_i^{\mathrm{BB},a} + U_i^{\mathrm{TT},a} + U_i^{\mathrm{SB},a} + U_i^{\mathrm{ST},a} + U_i^{\mathrm{BT},a}, \tag{13}$$

where the SS, BB, and TT terms are the potentials from bond stretches, bond angle bends, and torsions, and the SB, ST, and BT terms are the potentials from stretch–bend couplings, stretch–torsion couplings, and bend–torsion couplings, respectively. The force constant matrices in the terms of eqn (13) are respectively called $\mathbf{F}_i^{\mathrm{SS},a}$, $\mathbf{F}_i^{\mathrm{BB},a}$, $\mathbf{F}_i^{\mathrm{TT},a}$, $\mathbf{F}_i^{\mathrm{SB},a}$, $\mathbf{F}_i^{\mathrm{ST},a}$, and $\mathbf{F}_i^{\mathrm{BT},a}$.

In the current application of APRP to the construction of diabatic PESs of phenol, instead of using simple internal displacements $\mathbf{Q}_i^{[a]}$, we used variables with better global behaviors.

For bond stretches, instead of $r - r_{\mathrm{e}}$, we use $R = (r - r_{\mathrm{e}})/r$. This coordinate was originally proposed by Simons, Parr and Finlan (SPF)[77] for diatomic molecules. The use of SPF coordinates includes anharmonic effects and corrects the over-repulsion for large bond length ($r > r_{\mathrm{e}}$) and under-repulsion for short bond length ($r < r_{\mathrm{e}}$) of widely used force fields using $r - r_{\mathrm{e}}$.

For bond angle bends, instead of $\theta - \theta_{\mathrm{e}}$, we use $\cos\theta_{\mathrm{e}} - \cos\theta$ to preserve the continuity when the bond angle crosses π.

For torsions, $\phi - \phi_{\mathrm{e}}$ is replaced with $\sin\frac{n(\phi - \phi_{\mathrm{e}})}{2}$ or $\sin n(\phi - \phi_{\mathrm{e}})$ (depending on whether it is a diagonal or off-diagonal term) to maintain the correct periodicity behavior, where n is an integer number that indicates the local periodicity of the torsion. For phenol, the torsions in the phenoxyl ring all have $n = 1$.

With the new choice of variables, the terms in eqn (13) can be written explicitly as

$$U_i^{\mathrm{SS},a} = \frac{1}{2}\sum_{j=1}^{N_{\mathrm{S}}} k_{jj,i}^{\mathrm{SS},a}\left(\frac{r_j - r_{\mathrm{e},ji}^{[a]}}{r_j}\right)^2 + \frac{1}{2}\sum_{j=1}^{N_{\mathrm{S}}}\sum_{k\neq j}^{N_{\mathrm{S}}} k_{jk,i}^{\mathrm{SS},a}\left(\frac{r_j - r_{\mathrm{e},ji}^{[a]}}{r_j}\right)\times\left(\frac{r_k - r_{\mathrm{e},ki}^{[a]}}{r_k}\right), \tag{14a}$$

$$U_i^{\mathrm{BB},a} = \frac{1}{2}\sum_{j=1}^{N_{\mathrm{B}}} k_{jj,i}^{\mathrm{BB},a}\left(\cos\theta_j - \cos\theta_{\mathrm{e},ji}^{[a]}\right)^2 + \frac{1}{2}\sum_{j=1}^{N_{\mathrm{B}}}\sum_{k\neq j}^{N_{\mathrm{B}}} k_{jk,i}^{\mathrm{BB},a}\left(\cos\theta_{\mathrm{e},ji}^{[a]} - \cos\theta_j\right)\left(\cos\theta_{\mathrm{e},ki}^{[a]} - \cos\theta_k\right), \tag{14b}$$

$$U_i^{\mathrm{TT},a} = \frac{1}{2}\sum_{j=1}^{N_{\mathrm{T}}} k_{jj,i}^{\mathrm{TT},a}\sin^2\frac{n_j\left(\phi_j - \phi_{\mathrm{e},ji}^{[a]}\right)}{2} + \frac{1}{2}\sum_{j=1}^{N_{\mathrm{T}}}\sum_{k\neq j}^{N_{\mathrm{T}}} k_{jk,i}^{\mathrm{TT},a}\sin n_j\left(\phi_j - \phi_{\mathrm{e},ji}^{[a]}\right)\sin n_k\left(\phi_k - \phi_{\mathrm{e},ki}^{[a]}\right), \tag{14c}$$

$$U_i^{\mathrm{SB},a} = \sum_{j=1}^{N_{\mathrm{S}}}\sum_{k=1}^{N_{\mathrm{B}}} k_{jk,i}^{\mathrm{SB},a}\frac{r_j - r_{\mathrm{e},ji}^{[a]}}{r_j}\left(\cos\theta_{\mathrm{e},ki}^{[a]} - \cos\theta_k\right), \tag{14d}$$

$$U_i^{\mathrm{ST},a} = \sum_{j=1}^{N_{\mathrm{S}}}\sum_{k=1}^{N_{\mathrm{T}}} k_{jk,i}^{\mathrm{SB},a}\frac{r_j - r_{\mathrm{e},ji}^{[a]}}{r_j}\sin n_k\left(\phi_k - \phi_{\mathrm{e},ki}^{[a]}\right), \tag{14e}$$

$$U_i^{\mathrm{BT},a} = \sum_{j=1}^{N_{\mathrm{B}}}\sum_{k=1}^{N_{\mathrm{T}}} k_{jk,i}^{\mathrm{BT},a}\left(\cos\theta_{\mathrm{e},ji}^{[a]} - \cos\theta_j\right)\sin n_k\left(\phi_k - \phi_{\mathrm{e},ki}^{[a]}\right). \tag{14f}$$

Note that in eqn (14c), $\sin\frac{n(\phi - \phi_{\mathrm{e}})}{2}$ is used to build the local periodicity for the diagonal terms, while $\sin n(\phi - \phi_{\mathrm{e}})$ is used to replace $\phi - \phi_{\mathrm{e}}$ in cross terms.

The force constants in eqn (14a)–(14f) are related to the Hessian elements in eqn (13) by

$$k_{jk,i}^{\mathrm{SS},a} = F_{jk,i}^{\mathrm{SS},a} r_{\mathrm{e},ji}^{[a]} r_{\mathrm{e},ki}^{[a]},$$

$$k_{jk,i}^{\mathrm{BB},a} = \frac{F_{jk,i}^{\mathrm{BB},a}}{\sin\theta_{\mathrm{e},ji}^{[a]}\sin\theta_{\mathrm{e},ki}^{[a]}},$$

$$k_{jj,i}^{\mathrm{TT},a} = \frac{4F_{jj,i}^{\mathrm{TT},a}}{{n_j}^2},$$

$$k_{jk,i}^{\mathrm{TT},a} = \frac{F_{jk,i}^{\mathrm{TT},a}}{n_j n_k}\ \text{for}\ j\neq k,$$

$$k_{jk,i}^{\mathrm{SB},a} = \frac{F_{jk,i}^{\mathrm{SB},a} r_{\mathrm{e},ji}^{[a]}}{\sin\theta_{\mathrm{e},ki}^{[a]}},$$

$$k_{jk,i}^{\mathrm{ST},a} = \frac{F_{jk,i}^{\mathrm{ST},a} r_{\mathrm{e},ji}^{[a]}}{n_k},$$

and

$$k_{jk,i}^{\mathrm{BT},a} = \frac{F_{jk,i}^{\mathrm{BT},a}}{\sin\theta_{\mathrm{e},ki}^{[a]} n_k}.$$

With our new choice of variables to describe bond stretches, bond angle bends, and torsions, eqn (14) have much better behavior than the terms used previously for large distortions, although they require no more information. Thus, we recommend using them to construct force fields in the future. In addition to the above terms, we added a repulsive Born–Mayer potential between all pairs (1–4, 2–5, and 3–6) of *para* carbon atoms to all three diabatic potentials (see Fig. 1 for atomic numbering); this prevents the nonbonded atoms from getting too close during trajectories. The Born–Mayer potential is given as

$$V_{\mathrm{BM}} = B \sum_{\mathrm{X-Y}=1-4,2-5,3-6} \exp(-\alpha r_{\mathrm{X-Y}}) \tag{15}$$

where the interaction parameters are taken from the literature:[78] B is 42000 kcal mol^{-1}, and α is 3.58 Å^{-1}.

2.2. Diabatic couplings

In a similar spirit to that used in the APRP representations of the diabatic potentials, the diabatic couplings are expressed as

$$U_{ij} = U_{ij}^{[3,\mathbf{S}]}(\mathbf{S}|r) + U_{ij}^{[2,\phi]}(\phi|r), \tag{16}$$

where $U_{ij}^{[2,\phi]}$ is fitted to MC-QDPT data, and $U_{ij}^{[3,\mathbf{S}]}$ is constructed by interpolating linear expansions around anchor structures with tent functions:

$$U_{ij}^{[3,\mathbf{S}]} = \sum_{a=1}^{N_{\mathrm{A}}} \left(U_{ij,a}^{[0]} + \sum_{\alpha=1}^{9} A_{ija\alpha} S_\alpha \right) T_a(r), \tag{17}$$

where $U_{ij,a}^{[0]}$ is a constant parameter for anchor structure a, and $T_a(r)$ is the tent function with the same form as $T_i^{[a]}(r)$ used for tertiary potential. The parameter $A_{ija\alpha}$ in the representation of diabatic coupling U_{ij} equals the first partial derivative of U_{ij} with respect to S_α at anchor structure a. Four planar anchor points with other geometric parameters fixed at CASSCF/aug-cc-pVTZ optimized ground state minimum were chosen along the O–H dissociation coordinate, and they are the same for all diabatic couplings: r = 0.964, 1.32, 2.26, and 5.00 Å.

The diabatic coupling U_{12} of diabatic state U_1 ($^1\pi\pi$) to diabatic state U_2 ($^1\pi\pi^*$) is less important than the other couplings since the energy separation between those two states is quite large at all considered geometries. Therefore we used a simpler treatment for this coupling. In particular, we set all $A_{12a\alpha}$ parameters equal to zero, and we set $U_{12,3}^{[0]}$ and $U_{12,4}^{[0]}$ equal to zero; we set $U_{12,1}^{[0]} = -0.02$ eV, and we set $U_{12,2}^{[0]} = -0.03$ eV.

By symmetry, there is no contribution to diabatic couplings U_{13} and U_{23} from the in-plane vibrational coordinates of planar phenol. So we need only consider the contribution of out-of-plane modes to the diabatic couplings U_{13} and U_{23}. Phenol has ten out-of-plane coordinates, nine in the phenoxyl ring plus the C2–C1–O–H torsion ϕ. The nine out-of-plane phenoxyl coordinates we use (labeled S_1 to S_9) are similar to those used by Pongor *et al.*[79] These coordinates are given in Table 1.

Since the diabatic coupling matrix elements U_{23} and U_{13} are important near the first conical intersection (near anchor point 2) and the second conical intersection (near anchor point 3), respectively, the gradients $A_{23a\alpha}$ (α = 1 to 9) and $A_{13a\alpha}$ (α = 1 to 9) were calculated numerically (with a step size of 10 degree) from MC-QDPT/jul-cc-pVDZ fourfold-way calculations for anchor points 2 and 3, respectively. The gradients of diabatic couplings were set to zero for anchor points away from the relevant conical intersections.

To fit $U_{13}^{[2,\phi]}$ and $U_{23}^{[2,\phi]}$, flexible and general functional form needs to be used. As discussed previously, both of these couplings are zero at $\phi = 0^\circ$ due to symmetry. At $\phi = 90^\circ$, the phenol molecule also has C_s symmetry and in this case, three diabatic states U_1 ($^1\pi\pi$), U_2 ($^1\pi\pi^*$), and U_3 ($^1\pi\sigma^*$) belong to A', A'', and A', respectively. Only $U_{23}^{[2,\phi]}$ would be zero at $\phi = 90^\circ$ due to symmetry. We use the following functional forms to fit $U_{13}^{[2,\phi]}$ and $U_{23}^{[2,\phi]}$

$$U_{13}^{[2,\phi]} = \sum_{\eta=1}^{3} a_\eta(r) \sin^{2\eta-1}\phi, \tag{18a}$$

$$U_{23}^{[2,\phi]} = \sum_{\eta=1}^{3} a_\eta(r) \sin 2\eta\phi, \tag{18b}$$

where $a_\eta(r)$ is fitted with a linear combination of N Gaussians:

$$a_\eta = \sum_{m=1}^{N} A_{\eta,m} \exp\left[-\alpha_{\eta,m}(r - r_{\eta,m})^2\right] \tag{19}$$

Three Gaussian functions were used to fit a_1 in eqn (18a), and two Gaussian functions were used to fit a_2 and a_3 in eqn (18a). All a_η (η = 1, 2, and 3) in eqn (18b) were fitted with one Gaussian function.

2.3. Adiabatic potentials and nonadiabatic couplings

With diabatic potentials and couplings fitted in internal coordinates, the analytic Cartesian gradients of diabatic potentials and diabatic couplings $\nabla_n U_{ij}$ (n = 1, …, 3N) are evaluated straightforwardly by using Wilson **B**-matrices.[64] The adiabatic potential energies V_i are the eigenvalues of diabatic potential

Table 1 Out-of-plane coordinates of phenoxyl

Coordinate	Definition
δ_1	C2–C1–C6–C5 torsion
δ_2	C1–C6–C5–C4 torsion
δ_3	C6–C5–C4–C3 torsion
δ_4	C5–C4–C3–C2 torsion
δ_5	C4–C3–C2–C1 torsion
δ_6	C3–C2–C1–C6 torsion
S_1	$6^{-1/2}(\delta_1 - \delta_2 + \delta_3 - \delta_4 + \delta_5 - \delta_6)$
S_2	$12^{-1/2}(-\delta_1 + 2\delta_2 - \delta_3 - \delta_4 + 2\delta_5 - \delta_6)$
S_3	$4^{-1/2}(-\delta_1 + \delta_3 - \delta_4 + \delta_6)$
S_4	O7 out-of-plane bend
S_5	H12 out-of-plane bend
S_6	H11 out-of-plane bend
S_7	H10 out-of-plane bend
S_8	H9 out-of-plane bend
S_9	H8 out-of-plane bend

energy matrix **U**. The analytic Cartesian gradients of the adiabatic potentials and the nonadiabatic couplings are[34]

$$\nabla_n V_i = \sum_{j,k} c_{ij}^* c_{jk} \nabla_n U_{jk}, \quad (20)$$

and

$$\mathbf{F}_{ij} = \begin{cases} \dfrac{1}{V_j - V_i} \sum_{k,l} c_{ik}^* c_{jl} \nabla_n U_{kl} & (i \neq j) \\ 0 & (i = j) \end{cases}, \quad (21)$$

where $n = 1, \ldots, 3N$ and c_{ij} is the element of orthogonal matrix **C** that diagonalizes the diabatic potential matrix **U**.

2.4. Further information about the surfaces and couplings

Full details of the development of the APRP method and the optimized parameters are given in the supplementary material.[80] A Fortran subroutine that provides the diabatic potential energy surface matrices and their analytic derivatives, adiabatic potential energies and their analytic derivatives, and nonadiabatic couplings is available in the POTLIB library.[81,82]

2.5. Additional computational details

The reference orbitals and diabatic prototypes employed in the MC-QDPT fourfold-way diabatizations are specified in ref. 33. These calculations were performed with HONDOPLUS.[83]

For fitting the tertiary potential, the adiabatic partial optimizations and Hessian calculations at anchor points were performed by Kohn–Sham density functional theory with the M06-2X exchange-correlation functional and the jul-cc-pVDZ basis set with ultrafine grids by using Gaussian 09.[84]

The geometry optimizations and frequency analyses of equilibrium and transition structures were performed by the POLYRATE program[85] with the APRP surfaces. The geometry of the minimum energy conical intersection (MECI) between adiabatic states V_i and V_j was obtained by minimizing the penalty function $F = \frac{1}{2}(V_i + V_j) + \alpha(V_i - V_j)^2$ with $\alpha = 10^5\ E_h^{-1}$ (where $E_h = 1$ hartree).

We ran thousands of sample dissociative coupled-surface trajectories to confirm that the final versions of the coupled potential energy surfaces conserve energy and angular momentum and do not visit regions of configuration space where the surfaces yield unphysical results. These calculations were carried out with the ANT program.[86]

3. Results and discussion

3.1. Equilibrium geometries and frequencies

The bond lengths and bond angles of the $^1\pi\pi$ and $^1\pi\pi^*$ state of phenol and the $^2B_1$ and $^2B_2$ states of phenoxyl radical are given in Tables 2–4. For the $^1\pi\pi$ state of phenol, the experimental geometry is available by microwave spectroscopy[87] and electron-diffraction.[88] The geometry of the $^1\pi\pi^*$ state of phenol is available from simultaneous fit to the vibronic intensities and effective rotational constants.[89] No experimental bond lengths and bond angles are available for phenoxyl radical, and theoretical results[90] obtained by CASPT2 calculations with 9 active electrons in 8 active orbitals with the aug-cc-pVTZ basis set are listed for comparison. Due to the use of Born–Mayer repulsion of *para*-situated C atoms to avoid unphysical behavior in test trajectory calculations, the C–C bond lengths optimized with our APRP surface are slightly larger than the M06-2X results, but the tables show that both are in very good agreement with the literature[87–90] results. The C1–O bond of ground-state phenol is a typical single bond, having the bond length of 1.365 Å. The C–C bond lengths increase from ~1.40 Å in the ground state phenol to ~1.43 Å in the S_1 state of phenol, suggesting the benzene ring is expanded upon excited to the S_1 state.

The excited $^2B_2$ state of phenoxyl radical resembles the ground-state geometry of phenol (to which it connects diabatically) in that it has all C–C bond distances around 1.40 Å and a C1–O bond length of 1.33 Å. However, the equilibrium geometry of the ground state ($^2B_1$) of phenoxyl radical differs significantly from the geometries of both the $^1\pi\pi$ state of phenol and the $^2B_2$ state of phenoxyl radical. The ground state of phenoxyl radical has a geometry similar to that of a quinone, with much shorter C1–O bond length of 1.246 Å, and the C–C bond lengths are less symmetrical, with 1.461 Å for C1–C2 and C1–C6, 1.379 Å for C2–C3 and C5–C6, and 1.416 Å for C3–C4 and C4–C5, comparable to

Table 2 Calculated and experimental geometric parameters of the ground $^1\pi\pi$ state of phenol[a]

	APRP	M06-2X[b]	Microwave[c]	Electron-diffraction[d]
Bond lengths (Å)				
C1–C2	1.402	1.396	1.391	1.399
C2–C3	1.400	1.395	1.394	1.399
C3–C4	1.399	1.394	1.395	1.399
C4–C5	1.402	1.397	1.395	1.399
C5–C6	1.397	1.392	1.392	1.399
C6–C1	1.402	1.396	1.391	1.399
C2–H8	1.092	1.092	1.086	1.083
C3–H9	1.090	1.090	1.084	1.083
C4–H10	1.089	1.089	1.080	1.083
C5–H11	1.090	1.090	1.084	1.083
C6–H12	1.089	1.089	1.081	1.083
C1–O7	1.365	1.365	1.375	1.381
O7–H13	1.022	0.964	0.957	0.958
Bond angles (deg.)				
C6–C1–C2	120.4	120.4	120.9	121.6
C1–C2–C3	119.5	119.6	119.4	118.8
C2–C3–C4	120.6	120.6	120.5	120.6
C3–C4–C5	119.3	119.3	119.2	119.7
C4–C5–C6	120.8	120.8	120.8	120.6
C5–C6–C1	119.4	119.4	119.2	118.8
C1–C2–H8	120.0	120.0	120.0	
C2–C3–H9	119.3	119.3	119.5	
C3–C4–H10	120.3	120.3	120.3	
C4–C5–H11	119.9	119.9	119.8	
C5–C6–H12	121.7	121.7	121.6	
C6–C1–O7	117.1	117.1	117.0	117.2
C1–O7–H13	107.2	109.5	108.8	106.4

[a] See Fig. 1 for numbering of atoms. [b] jul-cc-pVDZ. [c] Ref. 87. [d] Ref. 88.

Table 3 Calculated and experimental geometric parameters of the $^1\pi\pi^*$ state of phenol[a]

	APRP	M06-2X[b]	Expt.[c]
Bond lengths (Å)			
C1–C2	1.434	1.429	1.421
C2–C3	1.424	1.419	1.420
C3–C4	1.427	1.421	1.431
C4–C5	1.425	1.419	1.425
C5–C6	1.426	1.421	1.426
C6–C1	1.425	1.420	1.413
C2–H8	1.090	1.090	1.083
C3–H9	1.087	1.087	1.080
C4–H10	1.090	1.091	1.079
C5–H11	1.087	1.087	1.080
C6–H12	1.087	1.087	1.079
C1–O7	1.338	1.338	1.356
O7–H13	1.034	0.967	0.992
Bond angles (deg.)			
C6–C1–C2	123.6	124.0	123.4
C1–C2–C3	117.5	117.3	118.5
C2–C3–C4	119.4	119.3	118.5
C3–C4–C5	122.4	122.7	123.1
C4–C5–C6	119.1	118.9	118.6
C5–C6–C1	118.0	117.8	118.4
C1–C2–H8	120.0	120.1	120.2
C2–C3–H9	120.7	120.8	
C3–C4–H10	118.7	118.5	
C4–C5–H11	120.2	120.2	
C5–C6–H12	123.3	123.4	122.3
C6–C1–O7	116.2	116.0	115.9
C1–O7–H13	106.5	109.5	108.8

[a] See Fig. 1 for numbering of atoms. [b] TD-DFT with the M06-2X functional and the jul-cc-pVDZ basis set. [c] Ref. 89.

Table 4 Calculated geometric parameters of the $\tilde{X}\ ^2B_1$ and $\tilde{A}\ ^2B_2$ states of phenoxyl radical[a]

	APRP	M06-2X[b]	CASPT2[c]
$\tilde{X}\ ^2B_1$ state			
Bond lengths (Å)			
C1–C2	1.461	1.453	1.448
C2–C3	1.379	1.375	1.379
C3–C4	1.416	1.410	1.408
C1–O7	1.246	1.249	1.255
C2–H8	1.090	1.090	1.081
C3–H9	1.090	1.090	1.081
C4–H10	1.090	1.090	1.081
Bond angles (deg.)			
C6–C1–C2	117.2	117.3	117.5
C1–C2–C3	120.8	120.8	120.7
C2–C3–C4	121.3	120.1	120.3
C1–C2–H8	116.9	116.9	117.1
C4–C3–H9	120.4	120.4	119.6
$\tilde{A}\ ^2B_2$ state			
Bond lengths (Å)			
C1–C2	1.409	1.403	1.402
C2–C3	1.397	1.392	1.393
C3–C4	1.400	1.394	1.394
C1–O7	1.331	1.333	1.330
C2–H8	1.088	1.088	1.079
C3–H9	1.090	1.090	1.081
C4–H10	1.088	1.088	1.079
Bond angles (deg.)			
C6–C1–C2	121.0	121.0	120.9
C1–C2–C3	118.7	118.7	118.9
C2–C3–C4	121.3	121.2	121.1
C1–C2–H8	119.6	119.6	119.7
C4–C3–H9	118.7	118.7	118.8

[a] See Fig. 1 for numbering of atoms. [b] jul-cc-pVDZ. [c] Ref. 90.

the C–O bond length (1.222 Å) and two C–C bond lengths (1.334, and 1.477 Å) in 1,4-benzoquinone.[91] The vibrational frequencies of the ground-state adiabatic surface were calculated at the minimum-energy geometries of the APRP surface, and they are compared in Fig. 3 to M06-2X frequencies and available experimental fundamental frequencies of phenol[92] and phenoxyl radical.[93] The frequencies calculated with our adiabatic PES reproduce the M06-2X results, both overestimating the experimental frequencies slightly. The overestimate by M06-2X is consistent with known trends,[94] but nevertheless we did not scale the density functional frequencies or Hessians in the present work.

3.2. Energetics and thermal adiabatic rate constants

The adiabatic vertical excitation energies of phenol and phenoxyl radical calculated with the APRP PESs are shown and compared with previous theoretical and available experimental results in Table 5. Experimentally, the spectrum for the optically allowed excitation of phenol from its ground state to the $^1\pi\pi^*$ state has a maximum at 4.58 eV.[95] The excitation to the $^1\pi\sigma^*$ state is electric dipole forbidden, and no reliable experimental result is available. Previous high-level *ab initio* studies suggested that the vertical excitation energy of the $^1\pi\sigma^*$ state should be in the range 5.6–5.9 eV.[33,44,51] Our APRP surface predicts vertical excitation energies to be 4.58 and 5.88 eV for excitations to the $^1\pi\pi^*$ state and the $^1\pi\sigma^*$ state, respectively, in good agreement with these reference values. In comparison to these results, the MC-QDPT/jul-cc-pVDZ results that were used in the construction of primary and secondary potential yield vertical excitation energies of 4.70 and 5.86 eV for the two states of phenol.[33] The slight difference between the APRP and MC-QDPT values is a result of the different equilibrium geometry of phenol used in the calculations. The CASSCF/aug-cc-pVTZ optimized geometry was used in the calculation with MC-QDPT while the equilibrium geometries of the APRP surface were used for the APRP result. The fact that the APRP agrees slightly better with the reference values is just a fortuitous result of this technical shift in geometric parameters.

The excitation energy of ground state phenoxyl radical to the $^2B_2$ state was first determined to be 1.06 eV in a gas-phase ultraviolet photoelectron spectroscopy experiment.[96] It was later observed to be 1.10 eV by UV-VIS and IR polarization spectroscopy of phenoxyl radical in cryogenic argon matrices.[97] The

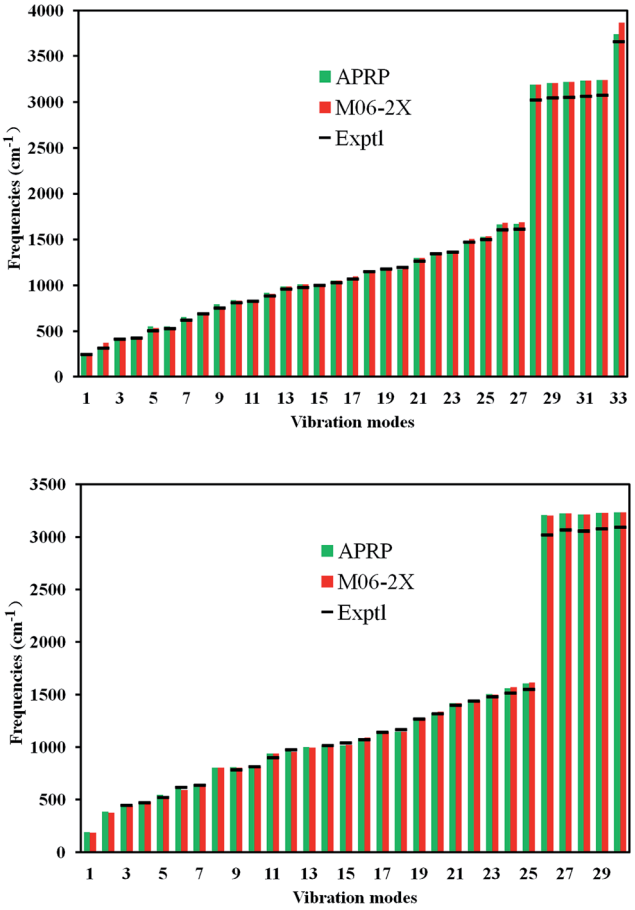

Fig. 3 Comparison of vibrational frequencies calculated from the ground-state APRP surface, from M06-2X calculations with available experimental results. Top: the $^1\pi\pi$ state of phenol; bottom: the $\tilde{X}\ ^2B_1$ state of phenoxyl radical.

excitation energy of phenoxyl radial from the $^2B_1$ state to the $^2B_2$ state calculated by our APRP surface is 1.07 eV, agreeing quite well with experimental results.

The equilibrium dissociation energy of the O–H bond calculated from the APRP PES is 3.93 eV, which is smaller than the experimentally derived D_e,[33,98,99] as shown in Table 5.

The classical adiabatic excitation energy, *i.e.*, the energy of the S_1 state minimum minus that of the S_0 state minimum on the APRP surfaces was calculated to be 4.42 eV. We can calculate the quantal adiabatic excitation energy, *i.e.*, the 0_0^0 energy, which is the energy of the S_1 zero point level minus that of the S_0 zero point level on the APRP surfaces, by adding the S_1 zero point energy (2.66 eV) and subtracting the S_0 zero point energy (2.85 eV); that yields 4.22 eV. This may be compared to the experimental value[51] of 4.51 eV.

Although there has been considerable emphasis on the location of the conical intersection, we should keep in mind that there is generally a saddle point on the lower adiabatic surface on the side of a conical intersection,[100] and for some purposes the characteristics of this saddle point are equally important or more important than the characteristics of the conical intersection. The transition state (*i.e.*, saddle point) for H dissociation on the first excited adiabatic state surface was located, with a classical barrier height of 0.72 eV with respect to the S_1 minimum (or 5.14 eV with respect to the S_0 minimum). At the saddle point geometry, the energies of the S_0 and S_2 states of phenol are 1.66 and 5.95 eV, respectively. The large energy gap (0.81 eV) between the S_1 and S_2 states at the saddle point suggests that an adiabatic model of dissociation on the S_1 surface might be a good zero-order model for the early dynamics of H-dissociation. The transition state has two nonplanar structures, which are mirror images of each other, with C2–C1–O–H torsion angles of −20.4 and 20.4°. As shown in Fig. 1, the C–C and C–O bond lengths in the transition state structures are very close to those in the ground state phenoxyl radical. The O–H bond length of the transition state structures is 1.33 Å, close to 1.32 Å at which value the S_1 and S_2 states of phenol intersect for planar geometry at the MC-QDPT level.[33] The imaginary frequency at the saddle point is $4271i$ cm^{-1}, which is rather high because the reduced mass for hydrogenic dissociation is low and because the saddle point is so close to a conical intersection. (A barrier due to a CI may be thin because the CI is pointy at the top, as compared to flat for a saddle point.) The minimum energy path in mass-scaled (*i.e.*, isoinertial) coordinates[101,102] (MEP) was calculated using the Page–McIver algorithm,[103] and the calculated potential energy V_{MEP}

Table 5 Vertical excitation energies of phenol and phenoxyl and the equilibrium dissociation energy of phenol (in eV)

	Phenol			Phenoxyl
	$^1\pi\pi^*$–$^1\pi\pi$	$^1\pi\sigma^*$–$^1\pi\pi$	D_e	$^2B_2$–$^2B_1$
APRP[a]	4.58	5.88	3.93	1.07
SA(3)-CAS(12,11)/jul-cc-pVDZ[b]	5.04	5.56	2.54	1.79
SA(3)-MC-QDPT(12,11)/jul-cc-pVDZ[b]	4.70	5.86	4.37	0.94
CC2/aug-cc-pVDZ[c]	4.86	5.36		
MRCI/aug-cc-pVDZ[d]	4.75	5.76		
CASPT2(10/10)/aug(O)-cc-pVTZ[e]	4.52	5.64	4.05	0.65
EOM-CCSD/aug(O)-cc-pVTZ[e]	4.97	5.67		
Experimental	4.58[f]		4.18[g]/4.08[g]	1.06[h]/1.10[i]

[a] The equilibrium geometries of phenol and phenoxyl radical were optimized with the APRP PES and were used to calculate the vertical excitation energies and the equilibrium dissociation energy for breaking the O–H bond. [b] Ref. 33. [c] Ref. 49. [d] Ref. 44. [e] Ref. 51. [f] Highest peak value obtained from ref. 95. [g] Derived in ref. 33 from ref. 98 (first value) and ref. 99 (second value). [h] Ref. 96. [i] Ref. 97.

along the MEP is shown in Fig. 4a. The abscissa of this figure is the reaction coordinate s, defined as the distance along the curved MEP through the isoinertial coordinates scaled to a reduced mass of 1 amu. We already noted the high imaginary frequency, which shows that the barrier is thin at the top, but Fig. 4a shows it is thin farther down as well. In fact, the V_{MEP} barrier of photodissociation of phenol on the S_1 excited state surface is much thinner than V_{MEP} curves of typical chemical reactions, consistent with the large imaginary frequency.

The zero point vibrational energy of the saddle point is 2.58 eV, as compared to the zero point vibrational energy of 2.66 eV for the equilibrium structure on S_1. The ground-state vibrationally adiabatic potential (V_a^G) curve is defined as the sum of V_{MEP} and the zero point energy of modes transverse to the reaction path; this potential is important because it serves as an effective potential energy for vibrationally adiabatic tunneling.[101,102,104–108] The ground-state vibrationally adiabatic barrier V_a^G along the S_1 surface of phenol is shown in Fig. 4b. The sum of the potential energy and the zero point energy at the saddle point is 3.30 eV, and the maximum value of this sum (*i.e.*, of the ground-state vibrationally adiabatic potential) is also 3.30 eV, and this occurs very close to the saddle, at $s = 0.004$ Å, where $r_{OH} = 1.32$ Å. Only two states ($n = 0$ and $n = 1$) of the O–H stretching mode have energies below the barrier as shown in Fig. 4b.

Fig. 4b can be used to illustrate the thinness of the effective barrier for tunneling by comparing it to that for the H + H_2 hydrogen-exchange reaction. The ground-state vibrationally adiabatic potential (V_a^G) curve for the H + H_2 reaction is shown in Fig. 3 of a previous paper.[109] In that figure, as in the present article, the reaction coordinate is scaled to 1 amu, so it is meaningful to compare the widths of the barriers. Examination of V_a^G for the H + H_2 reaction at an energy 0.10 eV below the barrier top shows a width of 0.7 Å, whereas the width of V_a^G in Fig. 4b at an energy 0.10 eV below the barrier top is only 0.12 Å, a factor of six thinner. This is certainly a dramatic difference. This may uncover a previously unappreciated general phenomenon, namely that barriers close to conical intersections may sometimes be very thin, allowing considerable tunneling on the lower surface at energies below the barrier.

Fig. 4c shows that the minimum energy reaction path is roughly divided into two stages, first the torsion angle changes with approximately constant O–H distance, then the O–H bond breaks at roughly constant torsion angle. If we consider the MEP in the downward direction, this means that the MEP approaches the minimum along the lowest-frequency normal mode, which is the expected result.[110,111] When the reaction path changes from the O–H stretch to the torsion, the potential energy barrier becomes more gradual (the rise from the equilibrium geometry is less steep along a low-frequency mode than along a high-frequency one). Although this change in character of the MEP and the associated V_{MEP} is interesting mechanistically, it has little effect on the tunneling because, as shown in Fig. 4, the change of character of the reaction path to become the torsion occurs for $s < -0.3$ Å, whereas the tunneling occurs in the region with $s > -0.3$ Å. If the change in character of the MEP were to occur at higher energy, the barrier would not retain its thin shape all the way down to the lowest tunneling energy.

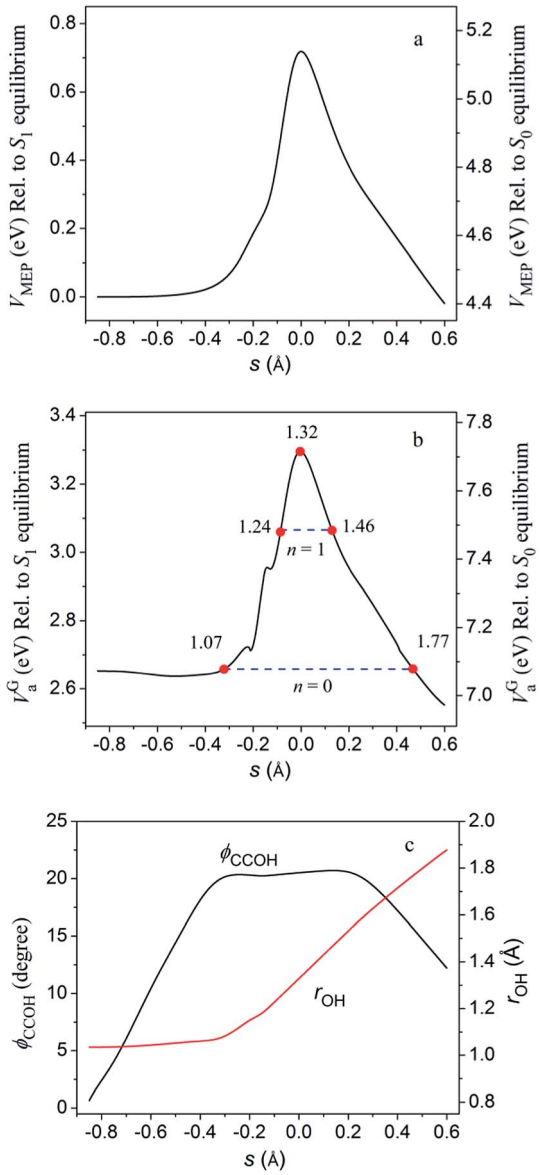

Fig. 4 (a) Calculated V_{MEP} *vs.* the reaction coordinate s (scaled to a reduced mass of one amu) for the O–H dissociation of phenol on the S_1 adiabatic surface. (b) Calculated ground-state vibrationally adiabatic potential (V_a^G) *vs.* the reaction coordinate s; the horizontal dashed lines labeled $n = 0$ and $n = 1$ denote the energy levels of the reaction coordinate mode (the O–H stretch) with vibrational quantum numbers of 0 and 1. The numbers denote the values of O–H bond length in Å at the termini of the classically forbidden regions for tunneling at these two energies. (c) Calculated O–H bond length and C2–C1–O–H torsion angle *vs.* the reaction coordinate s.

It is interesting to calculate the rate constants for the electronically adiabatic thermal dissociation of phenol to produce phenoxyl radical and H atom on the S_1 surface; such rate constants cannot be compared directly to experiment not only because the actually dissociation is not completely electronically adiabatic but also, and perhaps more significantly, because phenol need not become thermalized on the S_1 surface prior to dissociation. Nevertheless, the calculation – being the first calculation of the tunneling process to include all degrees

of freedom – provides valuable insight. The thermal rate constants of the unimolecular H-dissociation of phenol on the V_2 surface were calculated with canonical variational theory (CVT),[112,113] with vibrations transverse to the reaction coordinate quantized. Tunneling was included in the calculations by four different methods: the zero-curvature tunneling (ZCT) approximation,[101,114] the small-curvature tunneling (SCT) approximation,[108] the large-curvature tunneling (LCT) approximation,[115,116] and the microcanonically optimized tunneling (μOMT) approximation.[116,117] The ZCT calculation may be considered to be an approximation to the SCT one (as explained further below). The SCT calculations are vibrationally adiabatic and the LCT calculation is vibrationally nonadiabatic, and they also have different tunneling paths appropriate to the limits of small curvature of the reaction path and large curvature of the reaction path; the μOMT approximation chooses between them on the basis that, for each tunneling energy, the tunneling approximation that yields the most tunneling (largest rate constant) is expected to be most accurate.[118,119] Since only two vibrational states of the O–H stretching mode have energy levels below the barrier, we performed quantized-reactant-state tunneling calculations.[120,121] We found that the SCT and μOMT approximations give nearly the same result, both larger than the result given by LCT approximation. Therefore the SCT result is our most accurate, but we show both the ZCT and SCT results in Table 6 because the comparison is physically interesting. The ZCT result shows the effect of tunneling along the MEP as if it were a straight path in isoinertial coordinates, whereas the SCT result includes corner cutting across the concave side of the curved path to shorten the tunneling path and increase the tunneling probability. The unimolecular thermal rate constants increase by many orders of magnitude when one includes tunneling, and the effect of corner cutting is very significant.

The SCT tunneling probability in the $n = 0$ state of the O–H stretch (at an energy 2.66 eV above the equilibrium minimum of the S_1 potential) is 7.5×10^{-6}, and the SCT tunneling probability in the $n = 1$ state of the O–H stretch (at an energy of 3.07 eV) is 0.050.

Without considering the tunneling effect, the lifetime of the S_1 state, which is the reciprocal of the tabulated unimolecular rate constant, is calculated to be 3.2×10^7 ns at 300 K. Including tunneling by the SCT approximation, the lifetime is found to be between 0.4 and 5 ns for the temperatures shown in Table 6. Although we cautioned that the electronically adiabatic thermal lifetime cannot be compared directly to the photochemical lifetime, it is still interesting that the experimental lifetime of the S_1 state of phenol was reported to be $\tau \approx 2$ ns,[49] which shows that the calculation is not entirely unreasonable even if the remarkably good agreement of such an approximate calculation is partly fortuitous. Independent of this quantitative comparison though, the calculations show that without a doubt the dissociation reaction proceeds many orders of magnitude faster due to tunneling.

Table 6 Thermal unimolecular rate constants and lifetimes for hydrogen dissociation of phenol on the V_2 surface at various temperatures

T (K)	CVT	CVT/ZCT	CVT/SCT
Rate constant (s^{-1})			
150	7.8×10^{-10}	5.4×10^{6}	5.4×10^{8}
300	3.0×10^{1}	2.1×10^{6}	1.9×10^{8}
600	4.6×10^{6}	1.2×10^{8}	2.2×10^{8}
1000	5.6×10^{8}	1.8×10^{9}	2.4×10^{9}
Lifetime (ns)			
150	1.2×10^{18}	185	1.9
300	3.2×10^{7}	481	5.1
600	213	8.4	4.4
1000	1.8	0.6	0.4

3.3. Selected scans and 3D plots of conical intersections

Fig. 2 show the diabatic potential energy curves of three states, namely, the ground $^1\pi\pi$ state, the $^1\pi\pi^*$ state, and the repulsive $^1\pi\sigma^*$ state along the O–H stretch with the other geometric parameters fixed at the equilibrium geometry of ground-state phenol. As the O–H bond length increases, the APRP $^1\pi\sigma^*$ state intersects the $^1\pi\pi^*$ state at 1.32 Å (CI1); then it further intersects the $^1\pi\pi$ state at 2.23 Å (CI2), and it finally dissociates to the ground state of phenoxyl radical ($^2B_1$ state) and H atom. The $^1\pi\pi$ state, which is the ground state of phenol at short O–H bond length, intersects the $^1\pi\sigma^*$ state at 2.23 Å, and it dissociates to the excited state of phenoxyl radical ($^2B_2$ state) and H atom. MC-QDPT diabatic potential curves are also shown in Fig. 2 for comparison. The MC-QDPT curves cross at $r_{OH} \approx 1.32$ and 2.26 Å for $^1\pi\pi^*/^1\pi\sigma^*$ and $^1\pi\pi/^1\pi\sigma^*$.[33] Fig. 2 shows clearly that – despite the small difference in the location of CI2 – the APRP PES reproduces the MC-QDPT diabatic potential curves very well.

For planar geometry, the diabatic couplings are zero by symmetry, so the adiabatic states also intersect at $r = 1.316$ (CI1), where $V_2 = V_3 = 5.613$ eV and $r = 2.232$ Å (CI2) where $V_1 = V_2 = 4.434$ eV. Those points belong to the seams of conical intersections along which two adiabatic states are degenerate.

In Fig. 5, the diabatic potentials (U_1, U_2, and U_3) and diabatic couplings (U_{13} and U_{23}) are shown along the O–H bond stretch coordinate at various torsion angles ($\phi = 30$, 50, 70, and 90°). The diabatic potential curves calculated by fourfold way diabatization with MC-QDPT wave functions are also presented in Fig. 5 to show how well our PES reproduce both the calculated diabatic potentials and diabatic couplings. For a nonzero value of the C2–C1–O–H torsion angle, the diabatic potential U_3 still crosses U_2 and U_1 along the O–H bond stretch, but the C2–C1–O–H torsion breaks the planar symmetry and results in nonzero diabatic couplings, thus lifting the degeneracy all along the adiabatic curves and converting the intersections to avoided crossings. (Note that the term "avoided crossing" should not be understood as implying that surfaces do not cross;[32] rather it means that they do not cross along the path under discussion.) The only exception is at $\phi = 90°$, where the phenol molecule again has C_s symmetry, but now with the symmetry plane perpendicular to the benzene ring; diabatic states U_2 ($^1\pi\pi^*$) and

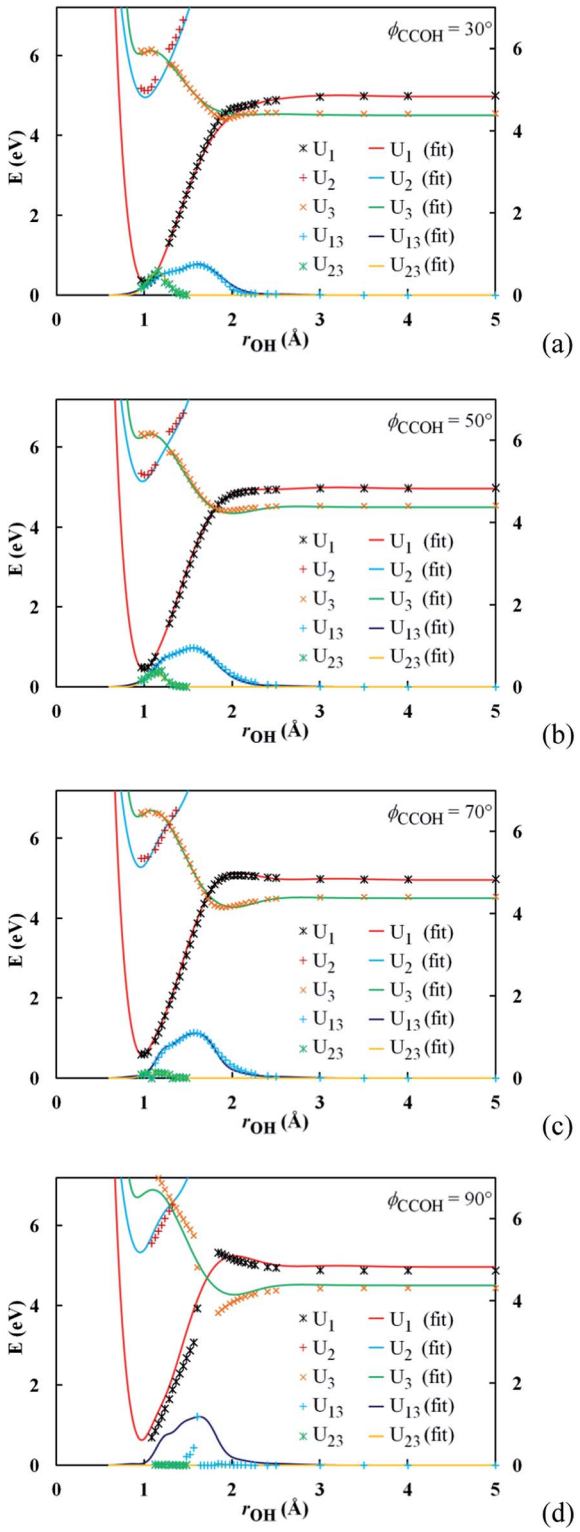

Fig. 5 Calculated and APRP diabatic potentials (U_1, U_2, and U_3) and diabatic couplings (U_{13} and U_{23}) of phenol along the O–H dissociation coordinate r at various C2–C1–O–H torsion angles ϕ. The other geometric parameters are fixed at their values at the equilibrium geometry of ground state phenol.

U_3 ($^1\pi\sigma^*$) now have A'' and A' symmetry, respectively, and the diabatic coupling U_{23} is zero by symmetry. Our PES yields zero diabatic coupling of U_{23} at $\phi = 90°$ by construction, shown in Fig. 5d.

Three-dimensional plots of diabatic surfaces U_2 and U_3 and adiabatic surfaces V_2 and V_3 are shown in Fig. 6 as functions of theO–H bond stretch and the C2–C1–O–H torsion coordinate with the other geometric parameters fixed with their values corresponding to the equilibrium structure of ground-state phenol. The diabatic states cross at both planar and non-planar geometries, forming a seam with $U_2 = U_3$ in the r and ϕ space. The diabatic coupling U_{23} is not zero for most nonplanar geometries, but it is zero along the $\phi = 0$ cut that intersects the diabatic intersection seam at $r = 1.316$ Å to yield a conical intersection there, this is simply another view of the CI1 intersection shown in Fig. 2. We should keep in mind that at $\phi = 90°$, U_{23} is zero along

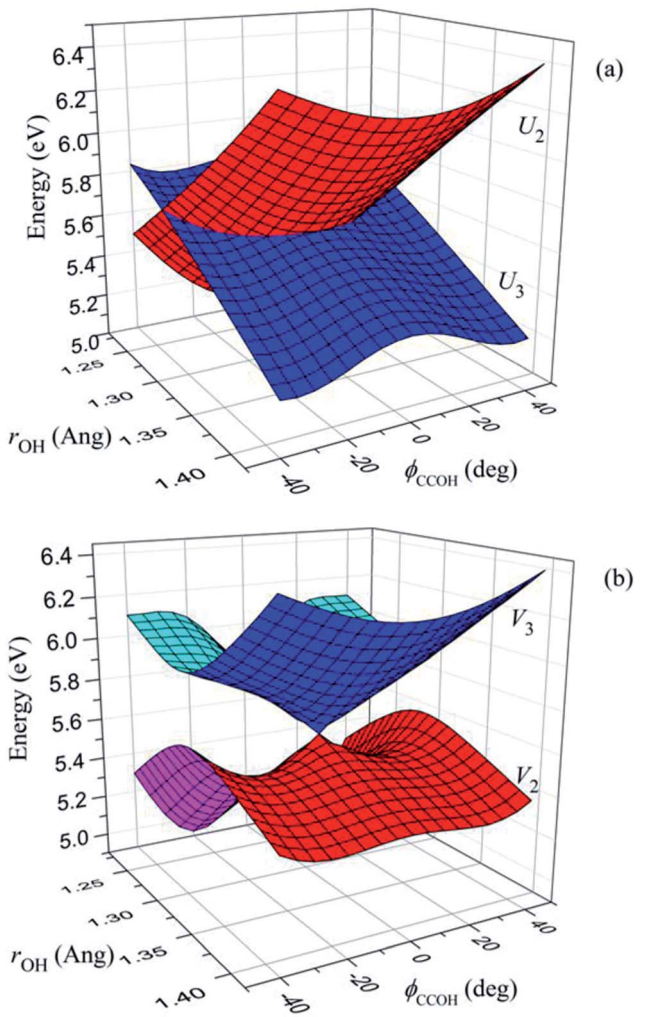

Fig. 6 Three-dimensional plots of (a) the U_2 and U_3 diabatic potential-energy surfaces showing the diabatic crossing of the $^1\pi\pi^*$ and $^1\pi\sigma^*$ states and (b) the V_2 and V_3 adiabatic potential-energy surfaces of phenol as functions of r and ϕ. The conical intersection (CI1) is seen at $r = 1.32$ Å and $\phi = 0°$ with all other geometric parameters fixed at the ground state equilibrium geometry of phenol.

the O–H bond stretching coordinate by symmetry, and there is another conical intersection with $V_2 = V_3$.

In Fig. 7, we also provide plots similar to Fig. 6 but now for U_1, U_3, V_1, and V_2. This provides another view of the intersection at $r = 2.232$ Å and $\phi = 0°$, labeled CI2 in Fig. 2. The ability to reproduce the conical intersection with our diabatic PES reflects one advantage of developing PESs in a diabatic representation – namely we do not have to fit the cusps in the adiabatic representation near conical intersections or to line up avoid crossings in the nearly degenerate adiabatic surfaces; these features emerge naturally from the diagonalization.

Although the conical intersections look like points in Fig. 6 and 7, we should keep in mind that these are just points on 31-dimensional intersection seams. The point with the lowest energy along a seam of conical intersections is called the minimum energy conical intersection (MECI), and its energy is an important characteristic of the coupled surfaces. With our analytic PESs, we located the MECI between V_2 and V_3 (MECI1) and the MECI between V_1 and V_2 (MECI2). Both MECIs have planar structures. MECI1 has $r_{OH} = 1.273$ Å with $V_2 = V_3 = 5.35$ eV and MECI2 has $r_{OH} = 1.971$ Å with $V_1 = V_2 = 4.17$ eV. The C–C, C–O, and O–H bond lengths and C–O–H bond angles of MECI1 and MECI2 are shown in Fig. 8, along with those of ground state phenol and phenoxyl radical. Both MECIs have C–C bond lengths similar to those in the ground-state phenoxyl radical equilibrium geometry, which corresponds to the diabatic state U_3 ($^1\pi\sigma^*$); these ring distortions lower the energy of the $^1\pi\sigma^*$ state with respect to what is shown in Fig. 2, and consequently the conical intersections have lower energies and shorter O–H bond lengths than the CIs in Fig. 2 (1.273 *vs.* 1.316 Å for the first CI and 1.971 *vs.* 2.231 Å for the second CI).

The energy of MECI1, 5.35 eV, is 0.21 eV higher than the saddle point discussed in the previous subsection. This small difference is consistent with the statement made there that the saddle point is close to a conical intersection and yet the gap between V_2 and V_3 increases from 0 to 0.81 eV as one moves from MECI1 to the V_2 saddle point, so the dynamics is much more adiabatic near the saddle point than near the CI. The displacement of the minimum energy path from the conical intersection does make the gap nonzero, but the gap is still much smaller than in the H + H_2 reaction where the gap at the saddle point is more than 6 eV.[122]

3.4. Diabatic couplings and adiabatic potentials for out-of-plane geometries

When out-of-plane modes are involved, the C_s symmetry of the phenol molecule is broken. The diabatic potential U_3 still crosses U_2 and U_1 along the O–H stretching coordinate, but the adiabatic potentials V_1, V_2, and V_3 need not intersect each other because of the non-zero diabatic couplings. Fig. 9 shows one-dimensional cuts through the potential surfaces for nonplanar geometries with the C2–C1–O–H torsion angle equal to ϕ =

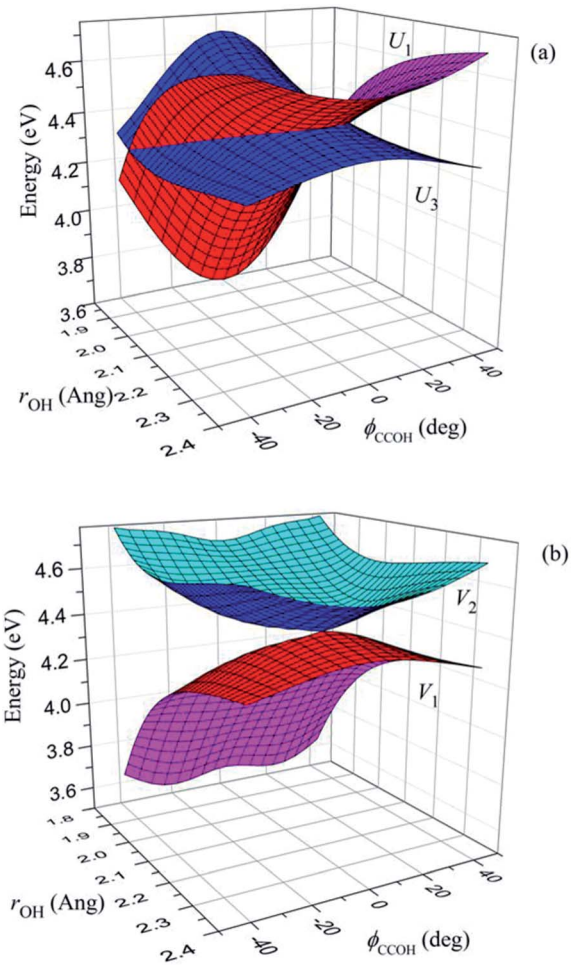

Fig. 7 Three-dimensional plots of (a) the U_1 and U_3 diabatic potential-energy surfaces showing the diabatic crossing of the $^1\pi\pi$ and $^1\pi\sigma^*$ states and (b) the V_1 and V_2 adiabatic potential-energy surfaces of phenol as functions of r and ϕ. The conical intersection (CI2) is seen at r = 2.23 Å and $\phi = 0°$ with all other geometric parameters fixed at the ground state equilibrium geometry of phenol.

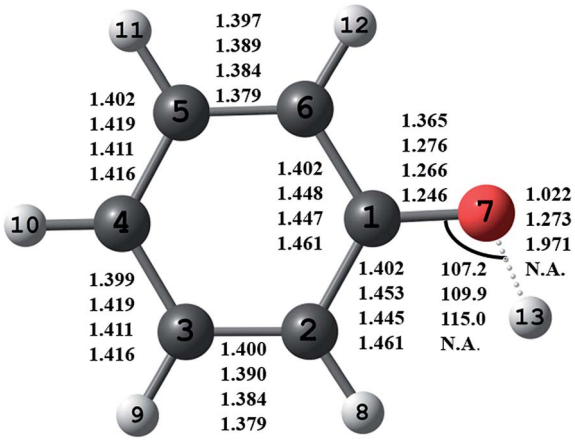

Fig. 8 The figure shows the structure of MECI1 and four sets of bond distances for key eight C–C, C–O, and O–H bond lengths (in Å) and the C–O–H bond angle (in degrees). From top to bottom are values for the equilibrium geometry of the S_0 state of phenol, MECI1, MECI2, and the $\tilde{X}\ ^2B_1$ state phenoxyl radical. "N.A." denotes not applicable.

145°. The phenoxyl ring is fixed at the ground state equilibrium geometry of phenol with $\theta_{COH} = 107°$ and 130° in Fig. 9a and b; the phenoxyl ring is fixed at the transition state geometry of the S_1 excited state with $\theta_{COH} = 112°$ in Fig. 9c; and the phenoxyl ring is fixed at the ground-state equilibrium geometry of phenoxyl radical with $\theta_{COH} = 115°$ in Fig. 9d. In all cases, the adiabatic potential curves show avoided intersections along the O–H stretching coordinate, as expected.

Near conical intersections, diabatic potential energy curves may cross along the C2–C1–O–H torsion coordinate. But adiabatic potential energy curves avoid crossing since the nonzero diabatic couplings lift the degeneracy of diabatic states. This is shown clearly in Fig. 10. In Fig. 10a, for $r_{OH} = 1.29$ Å with all other geometric parameters except ϕ fixed at the ground equilibrium geometry of phenol, the diabatic potential U_3 crosses U_2 at $\phi = 25°$, but the adiabatic potential curves V_2 and V_3 avoid crossing. In Fig. 10b, for $r_{OH} = 2.10$ Å, the diabatic potential U_3 crosses U_1 at $\phi = 24°$, but again the adiabatic potential curves V_1 and V_2 avoid crossing.

So far we have shown cuts through the APRP PESs for a fixed geometry of the phenoxyl moiety of phenol. The good performance of our APRP PES for those geometries is expected since we used general functional forms to fit the dependence of MC-QDPT diabatic potentials and couplings on the primary and secondary coordinates. Next we examine the PESs for some nonplanar geometries with distorted phenoxyl groups. In the language of the APRP, we are looking here at how the PESs and couplings vary for geometries with distortions in tertiary coordinates. In particular, we examine the dependence on the ν_{16a} (an out-of-plane ring puckering/twisting vibration of a″ symmetry) and ν_{16b} modes that have been singled out for attention in experimental studies.[46,51] (We use Wilson's labeling scheme[123] for the phenol and phenoxyl vibrational modes.)

The diabatic potentials and relevant diabatic couplings along Cartesian normal-mode displacements of the ν_{16a} and ν_{16b} modes were calculated with our APRP PESs and compared with MC-QDPT results at the two conical intersections in Fig. 11 and 12. The normalized Cartesian normal-mode displacements of ν_{16a} and ν_{16b} modes calculated by the M06-L functional[124] with the aug-cc-pVTZ basis set were used in order to be consistent with previous MC-QDPT calculations.[33] The APRP diabatic potentials and couplings agree qualitatively with the MC-QDPT results. The diabatic coupling U_{23} increases linearly along the Cartesian normal-mode displacements of both ν_{16a} and ν_{16b} modes at CI1. At CI2, the diabatic coupling U_{13} also increases linearly along the Cartesian normal-mode displacement of the ν_{16a} mode. However, it remains very small along the Cartesian normal-mode displacement of the ν_{16b} mode. These calculations of the diabatic couplings for out-of-plane distortion of the ring in phenol can be used in the future for full-dimensional studies of the effects of vibrational mode coupling on the dynamics of photodissociation of phenol. However, we can also gain insight into the photodissociation dynamics by studying the couplings even without carrying out full dynamics studies, and we consider that next.

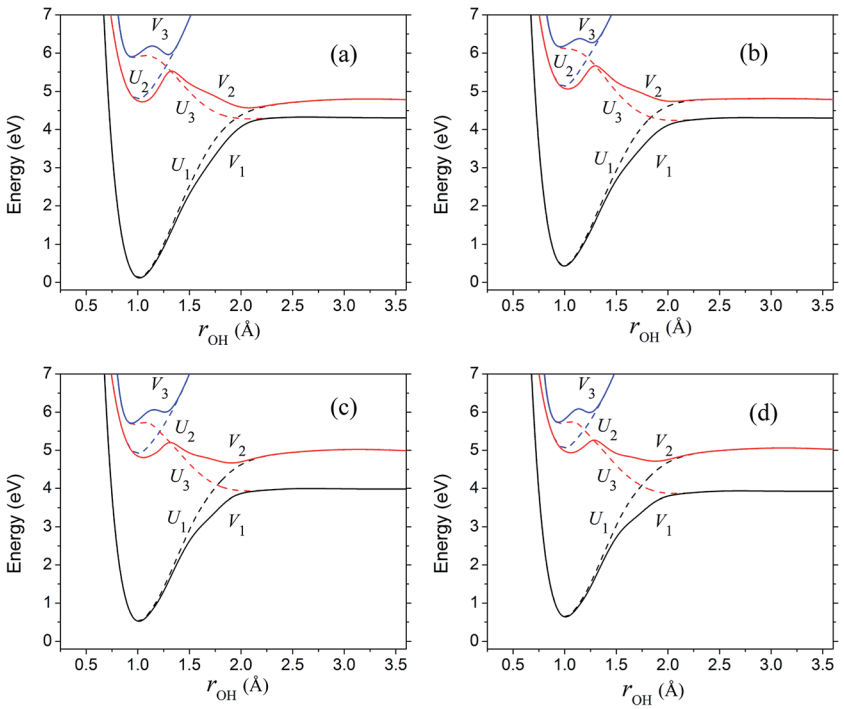

Fig. 9 Diabatic potentials (U_1, U_2, and U_3) and adiabatic potentials (V_1, V_2, and V_3) *versus* r_{OH} with C2–C1–O–H torsion $\phi_{CCOH} = 145°$, (a) all other geometric parameters fixed at the ground state equilibrium geometry of phenol, (b) $\theta_{COH} = 130°$ and all other geometric parameters fixed at the ground state equilibrium geometry of phenol, (c) all other geometric parameters fixed at the excited state (S_1) transition state geometry of phenol, (d) $\theta_{COH} = 115°$ and all other geometric parameters fixed at the ground state equilibrium geometry of phenoxyl radical.

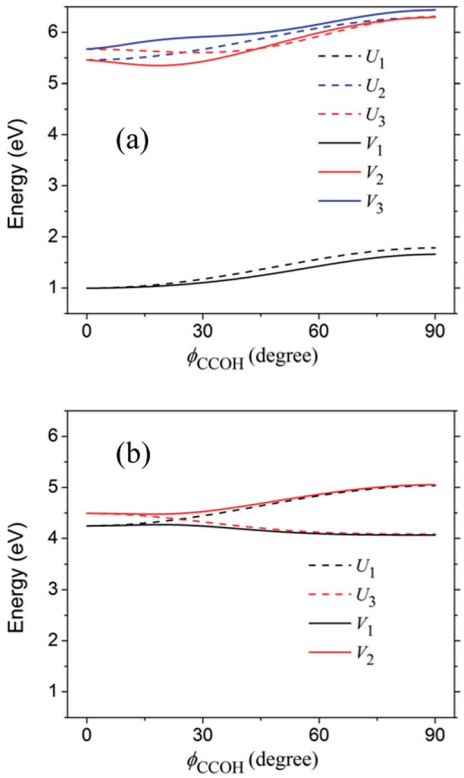

Fig. 10 Diabatic potentials (U_1, U_2, and U_3) and adiabatic potentials (V_1, V_2, and V_3) *versus* C2–C1–O–H torsion ϕ_{CCOH} (a) with $r_{OH} = 1.29$ Å and all other geometric parameters fixed at the ground state equilibrium geometry of phenol, (b) with $r_{OH} = 2.10$ Å and all other geometric parameters fixed at the ground state equilibrium geometry of phenol.

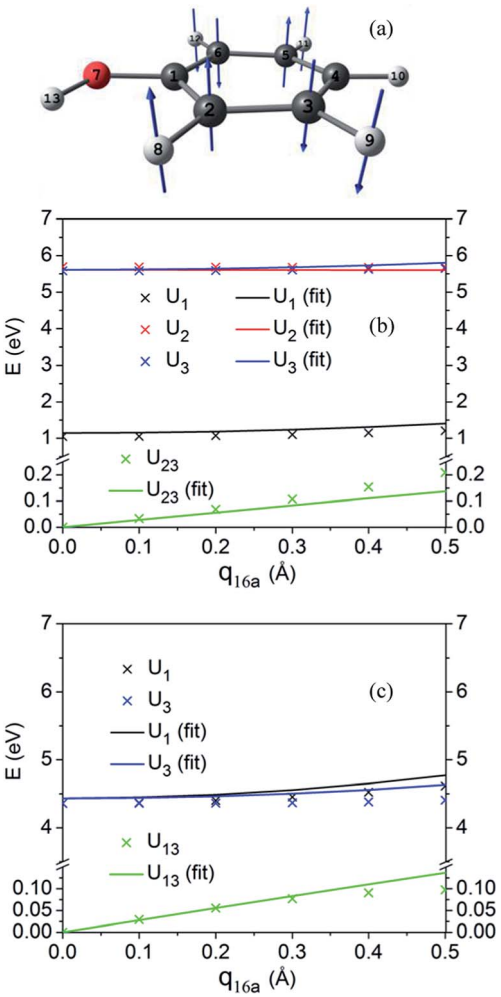

Fig. 11 The atomic displacements of vibrational mode ν_{16a} (a), and calculated and APRP diabatic potentials and the most relevant diabatic couplings at conical intersections of the $^1\pi\pi^*$ and $^1\pi\sigma^*$ states (b) and the $^1\pi\pi$ and $^1\pi\sigma^*$ states (c) along scaled Cartesian normal-mode displacements.

First we recall the Ehrenfest effective PES, which we will call $\bar{V}$, for multi-electronic-state molecular dynamics is a weighted average over the adiabatic PESs, V_j, where the weights are the diagonal elements, ρ_{jj}, of the electronic density matrix.[34,125–128] Then we consider a photoexcited system with $\rho_{22} \gg \rho_{11}$ and $\rho_{22} \gg \rho_{33}$ approaching CI1. If the system is not adiabatic, we expect to see ρ_{33} increase, and that puts a higher weight on V_3 and raises $\bar{V}$, which makes it less likely that the system dissociates. Now let the system undergo a vibration in an out-of-plane mode while it approaches CI1; this has two consequences: (1) the vibration causes U_2 and V_2 to go up, which raises $\bar{V}$, decreasing the probability of dissociation; and (2) the vibration causes $|U_{23}|$ to go up, which makes the system more adiabatic, which keeps ρ_{33} low, which tends to keep $\bar{V}$ low, which increases the probability of dissociation. For some modes, call them "inactive" modes, effect (1) may dominate. For other modes, call them "active" modes, effect (2) may dominate. We conclude that reaction will preferentially occur through those molecules that happen to have active modes excited as they get to CI1.

When one experimentally observes the products (as Ashfold and coworkers[46,51] do), one will then see an excess of molecules with active modes excited since those are the ones that preferentially reacted. Under the conditions of the experiments, most of the vibrational modes are initially in their ground vibrational state. Let q_m be an out-of-plane vibrational mode, and let Z_m be the zero point energy in that mode. Near a planar geometry,

$$U_2 = U_2(q = 0) + \frac{1}{2}k_m{q_m}^2, \quad (22)$$

and

$$U_{23} = C_m q_m, \quad (23)$$

where k_m is a force constant, and C_m depends on the fit to the diabatic couplings. (Both k_m and C_m depend on geometry in the APRP.) Let $D_m = |C_m|$, and let Q_m be the harmonic turning point of q_m:

$$Q_m = \sqrt{2Z_m/k_m}, \quad (24)$$

Since an active mode has $|U_{23}|$ large and $U_2(Q_m) - U_2(0)$ small, we define

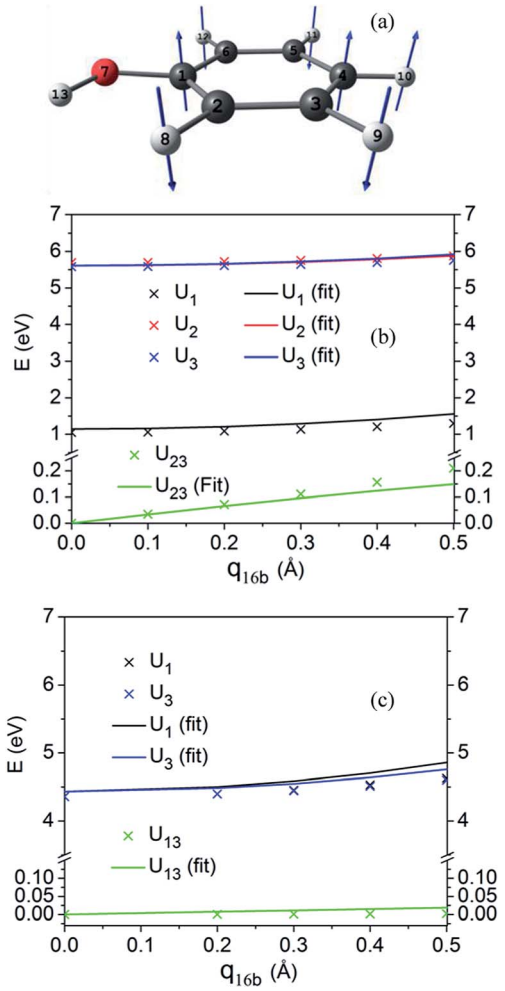

Fig. 12 The atomic displacements of vibrational mode ν_{16b} (a), and calculated and APRP diabatic potentials and the most relevant diabatic couplings at conical intersections of the $^1\pi\pi^*$ and $^1\pi\sigma^*$ states (b) and the $^1\pi\pi$ and $^1\pi\sigma^*$ states (c) along scaled Cartesian normal-mode displacements.

$$X(Q_m) \equiv \frac{|U_{23}(Q_m)|}{U_2(Q_m) - U_2(0)}. \quad (25)$$

Substituting eqn (22)–(25), we have

$$X(Q_m) = D_m \sqrt{2/k_m Z_m}. \quad (26)$$

This is the simplest unitless quantity that goes up when $|U_{23}|$ goes up and is larger when the rise in U_2 is smaller.

We calculated $X(Q_m)$ for all out-of-plane modes at a planar geometry of the S_1 state of phenol that has the same OH distance as the transition state but the rest of the coordinates are the same as in the equilibrium geometry of the S_1 state. We found that $X(Q_m)$ is 0.12 for mode ν_{16a} (103 cm^{-1}), 0.064 for mode 11 (197 cm^{-1}), and 0.050 for mode 10a (389 cm^{-1}), but it ranges between 0.013 and 2×10^{-4} for the other seven out-of-plane modes of phenol (with frequencies in the range 92–865 cm^{-1}). This provides a simple explanation for why ν_{16a} mode is the most prominent excited mode observed[46,51] in the products of the photodissociation reaction; and we note that mode 10a is also observed[51] to be excited in the products. We note that vibrational modes can also be excited during the energy release phase as the system progresses from the region of the saddle point and CI1 down to products, but the analysis just given is consistent with the interpretation[51] of at least some of the observed vibrational mode selectivity as arising from the ability of various vibrational modes to promote state coupling. Unfortunately this is called promotion of "nonadiabatic transitions" in ref. 51, but actually—as the above discussion should make clear—the relevant consideration is promotion of diabatic coupling, which leads to adiabatic passage, not nonadiabatic transitions.

3.5. Nonplanar conical intersections

The conical intersections occur in a $(3N - 8)$-dimensional manifold, where N is the number of atoms. Thus, in phenol molecule, the conical intersection should have a dimension of 31. Both U_{13} and U_{23} vanish for planar geometries, which form a 23-dimensional manifold, because $2N - 3 = 23$. With the further constraint of $U_2 = U_3$ or $U_1 = U_3$, the $^1\pi\pi^*/^1\pi\sigma^*$ and $^1\pi\pi/^1\pi\sigma^*$ conical intersections occur in a 22-dimensional manifold in planar geometry. This is a relatively low-dimensional subset of the full 31-dimensional seam, and therefore most of the conical intersection seam has nonplanar geometry.

Locating conical intersections that are not determined by symmetry can be carried out by special algorithms in the adiabatic representation.[129,130] However, with the analytic diabatic PES matrices of phenol on hand, we can locate such conical intersections more easily.[131,132] Contour plots of $U_2 - U_3$ and U_{23} with respect to the C2–C1–O–H torsion angle ϕ and one of the H out-of-plane bend angles, in particular $\theta_{8-2-1-3}$, which denotes the deviation of atom 8 from the 2–1–3 plane, are shown in Fig. 13 at $r = 1.29$ Å. At the planar geometries, both ϕ and $\theta_{8-2-1-3}$ are zero, and adiabatic state V_3 is 0.21 eV higher in energy than adiabatic state V_2. The seam with $U_{22} = U_{33} = 0$ and the seam with $U_{23} = 0$ cross at $\phi = 40.1°$ and $\theta_{8-2-1-3} = 25.0°$. If these two diabatic states formed a closed space, that point (solid circle in Fig. 13) will be a nonplanar conical intersection of V_2 and V_3, but due to the perturbation by diabatic state U_1, the location of the true conical intersection is displaced from this point. Nevertheless this is a good starting point for a search, and by making a contour plot of $V_2 - V_3$ in this vicinity (which is inexpensive because we have an analytic representation), we find that $V_2 = V_3 = 5.93$ eV at $\phi = 49.3°$ and $\theta_{8-2-1-3} = 15.8°$ (solid square in Fig. 13).

In Fig. 14, we present the contour plots of $U_1 - U_3$ and U_{13} with respect to the C2–C1–O–H torsion angle ϕ and one of the H out-of-plane bend angles $\theta_{9-3-2-4}$ at $r = 2.20$ Å. The seam with $U_1 - U_3 = 0$ eV and the seam with $U_{13} = 0$ eV cross at $\phi_{2-1-7-13} = 12.4°$ and $\theta_{9-3-2-4} = -16.2°$ which is also a nonplanar conical intersection with $V_1 = V_2 = 4.54$ eV as a result of the smallness of the perturbation by diabatic state U_2 at this geometry.

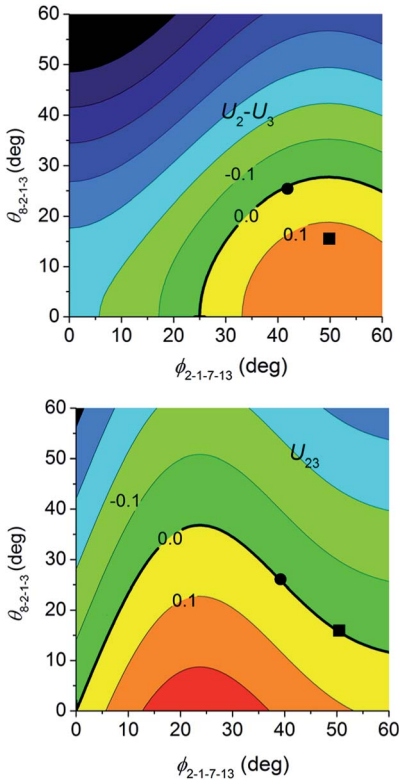

Fig. 13 Contour plots of $U_2 - U_3$ and U_{23} (in eV) to locate the nonplanar conical intersection of the $^1\pi\pi^*$ and $^1\pi\sigma^*$ states at $r_{OH} = 1.29$ Å. The solid square and circle are explained in Section 3.5.

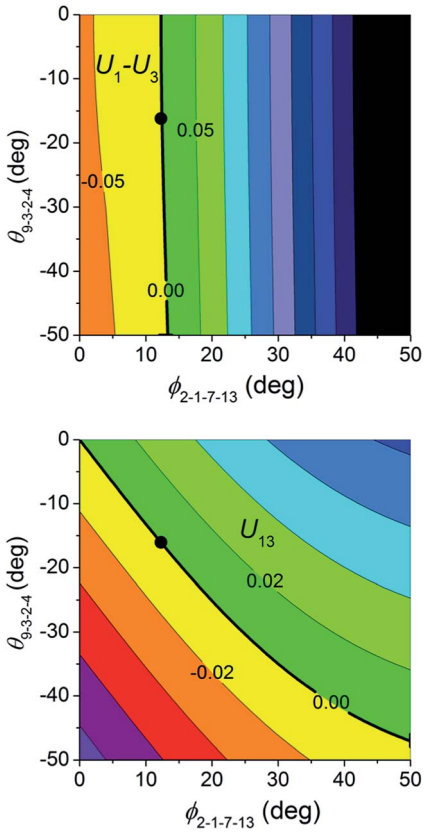

Fig. 14 Contour plots of $U_1 - U_3$ and U_{13} (in eV) to locate the nonplanar conical intersection of the $^1\pi\pi$ and $^1\pi\sigma^*$ states at $r = 2.20$ Å.

4. Summary and concluding remarks

Photochemical reactions and other light-induced processes involving electronically excited states are important for synthesis and a myriad of other applications, but theoretical understanding has lagged that for thermal reactions. In this paper we take steps to try to improve this situation. First, using on a new method, we present fully analytic coupled potential energy surfaces and their couplings, based on high-level electronic structure calculations for a system with a large number (33) of internal degrees of freedom. These surfaces are based on an improved version of the APRP method that uses internal coordinates with better global behavior than the usual internal coordinates. For the three-state photodissociation of phenol, we have used the improved APRP method to develop analytic full-dimensional diabatic potential energy surfaces not only for the surfaces and their analytic gradients, but also for analytic diabatic coupling surfaces and their gradients; by transformation the method then yields adiabatic energy surfaces and their gradients and nonadiabatic momentum couplings.

Selected scans show that our APRP diabatic PESs and diabatic coupling surfaces reproduce well the results calculated previously by the fourfold way with the MC-QDPT method. We illustrate the magnitudes of the diabatic couplings and adiabatic gaps for various nonplanar geometries and show how they may be used to provide a simple estimate of which vibrational modes promote the dissociation process. By diagonalizing the diabatic potential matrices, conical intersections can be correctly reproduced, and we show how to use the APRP potential matrix to locate points on conical intersection seams at nonsymmetrical geometries.

We used the APRP potentials to locate the transition state, minimum-energy path, and vibrationally adiabatic potential energy curve for electronically adiabatic photodissociation of phenol on the S_1 surface and to study of thermal rate constants for adiabatic dissociation, which confirmed the importance of tunneling for S_1 state photodissociation of phenol.

The APRP potential for phenol can be used for the study of dynamics of photodissociation of phenol to elucidate the effect of ring motion, including out-of-plane vibrational modes. The success of the APRP method in producing coupled surfaces and couplings suitable for full-scale dynamics calculations is encouraging because the method is very general, and the improved APRP method can be used to map out coupled potential energy surfaces and their couplings for other complex systems, thereby allowing much more complete molecular dynamics simulations than have been practical in the past.

Acknowledgements

The authors are grateful to Rubén Meana-Pañeda for helpful discussions of this work. This work was supported in part by the

U. S. Department of Energy, Office of Basic Energy Sciences, under SciDAC grant no. DE-SC0008666.

References

1 M. Born and R. Oppenheimer, *Ann. Phys.*, 1927, **84**, 457.
2 B. K. Kendrick, C. A. Mead and D. G. Truhlar, *Chem. Phys.*, 2002, **277**, 31.
3 A. W. Jasper, C. Zhu, S. Nangia and D. G. Truhlar, *Faraday Discuss.*, 2004, **127**, 1.
4 C. A. Mead and D. G. Truhlar, *J. Chem. Phys.*, 1982, **77**, 6090.
5 W. Lichten, *Phys. Rev.*, 1963, **131**, 229.
6 T. F. O'Malley, *J. Chem. Phys.*, 1969, **51**, 322.
7 B. C. Garrett and D. G. Truhlar, in *Theoretical Chemistry: Advances and Perspectives*, ed. D. Henderson, Academic Press, New York, 1981, vol. 6A, p. 215.
8 H.-J. Werner and W. Meyer, *J. Chem. Phys.*, 1981, **74**, 5802.
9 J. B. Delos, *Rev. Mod. Phys.*, 1981, **53**, 287.
10 D. Stahel, M. Leoni and K. Dressler, *J. Chem. Phys.*, 1983, **79**, 2541.
11 M. H. Alexander, *Chem. Phys.*, 1985, **92**, 337.
12 T. C. Thompson, D. G. Truhlar and C. A. Mead, *J. Chem. Phys.*, 1985, **82**, 2392.
13 T. Pacher, L. S. Cederbaum and H. Köppel, *J. Chem. Phys.*, 1988, **89**, 7367.
14 A. Boutalib and F. X. Gadéa, *J. Chem. Phys.*, 1992, **97**, 1144.
15 M. Marchi, J. N. Gehlen, D. Chandler and M. Newton, *J. Am. Chem. Soc.*, 1993, **115**, 4178.
16 Y. Mo and J. Gao, *J. Comput. Chem.*, 2000, **21**, 1458.
17 H. Nakamura and D. G. Truhlar, *J. Chem. Phys.*, 2001, **115**, 10353; H. Nakamura and D. G. Truhlar, *J. Chem. Phys.*, 2002, **117**, 5576; H. Nakamura and D. G. Truhlar, *J. Chem. Phys.*, 2003, **118**, 6816.
18 P.-H. Sit, M. Cococcioni and N. Marzari, *Phys. Rev. Lett.*, 2006, **97**, 28303.
19 O. Godsi, C. R. Evenhuis and M. A. Collins, *J. Chem. Phys.*, 2006, **125**, 104105.
20 G. A. Arteca and O. Tapia, *Int. J. Quantum Chem.*, 2007, **107**, 382.
21 F. D. X. George and S. Kumar, *J. Chem. Phys.*, 2007, **119**, 409.
22 B. N. Papas, M. S. Schuuman and D. R. Yarkony, *J. Chem. Phys.*, 2008, **129**, 124104.
23 J. E. Subotnik, S. Yeganeh, R. J. Cave and M. A. Ratner, *J. Chem. Phys.*, 2008, **129**, 244101.
24 T. Ichino, J. Gauss and J. F. Stanton, *J. Chem. Phys.*, 2009, **130**, 174105.
25 T. Voorhis, T. Kowalczak, B. Kaduk, L.-P. Wang, C.-L. Cheng and Q. Wu, *Annu. Rev. Phys. Chem.*, 2010, **61**, 149.
26 A. Sirjoosingh and S. Hammes-Schiffer, *J. Phys. Chem. A*, 2011, **115**, 2367.
27 E. Alguire and J. E. Subotnik, *J. Chem. Phys.*, 2011, **135**, 44114.
28 M. Pavanello and J. Neugebauer, *J. Chem. Phys.*, 2011, **135**, 134113.
29 Y. C. Park, H. An, H. Choi, Y. S. Lee and K. K. Baeck, *Theor. Chem. Acc.*, 2012, **131**, 1212.
30 X. Zhu and D. R. Yarkony, *J. Chem. Phys.*, 2012, **137**, 22A511.
31 K. R. Yang, X. Xu and D. G. Truhlar, *Chem. Phys. Lett.*, 2013, **573**, 84.
32 D. G. Truhlar and C. A. Mead, *Phys. Rev. A*, 2003, **68**, 32501.
33 X. Xu, K. R. Yang and D. G. Truhlar, *J. Chem. Theory Comput.*, 2013, **9**, 3612.
34 A. W. Jasper and D. G. Truhlar, in *Conical Intersections: Theory, Computation, and Experiment*, ed. W. Domcke, D. Yarkony and H. Köppel, World Scientific, Singapore, 2011, pp. 375–414.
35 A. L. Sobolewski and W. Domcke, *J. Phys. Chem. A*, 2001, **105**, 9275.
36 A. L. Sobolewski, W. Domcke, C. Dedonder-Lardeux and C. Jouvet, *Phys. Chem. Chem. Phys.*, 2002, **4**, 1093.
37 Z. Lan, W. Domcke, V. Vallet, A. L. Sobolewski and S. Mahapatra, *J. Chem. Phys.*, 2005, **122**, 224315.
38 M. N. R. Ashfold, B. Cronin, A. L. Devine, R. N. Dixon and M. G. D. Nix, *Science*, 2006, **312**, 1637.
39 C.-M. Tseng, Y. T. Lee, M.-F. Lin, C.-K. Ni, S.-Y. Liu, Y.-P. Lee, Z. F. Xu and M. C. Lin, *J. Phys. Chem. A*, 2007, **111**, 9463.
40 A. L. Devine, M. G. D. Nix, B. Cronin and M. N. R. Ashfold, *Phys. Chem. Chem. Phys.*, 2007, **9**, 3749.
41 G. A. King, A. L. Devine, M. G. D. Nix, D. E. Kelly and M. N. R. Ashfold, *Phys. Chem. Chem. Phys.*, 2008, **10**, 6417.
42 M. N. R. Ashfold, A. L. Devine, R. N. Dixon, G. A. King, M. G. D. Nix and T. A. A. Oliver, *Proc. Natl. Acad. Sci. U. S. A.*, 2008, **105**, 12701.
43 M. G. D. Nix, A. L. Devine, R. N. Dixon and M. N. R. Ashfold, *Chem. Phys. Lett.*, 2008, **463**, 305.
44 O. P. J. Vieuxmaire, Z. Lan, A. L. Sobolewski and W. Domcke, *J. Chem. Phys.*, 2008, **129**, 224307.
45 M. L. Hause, Y. H. Yoon, A. S. Case and F. F. Crim, *J. Chem. Phys.*, 2008, **128**, 104307.
46 G. A. King, T. A. A. Oliver, M. G. D. Nix and M. N. R. Ashfold, *J. Phys. Chem. A*, 2009, **113**, 7984.
47 A. Iqbal, M. S. Y. Cheung, M. G. D. Nix and V. G. Stavros, *J. Phys. Chem. A*, 2009, **113**, 8157.
48 M. N. R. Ashfold, G. A. King, D. Murdock, M. G. D. Nix, T. A. A. Oliver and A. G. Sage, *Phys. Chem. Chem. Phys.*, 2010, **12**, 1218.
49 A. Pino, A. N. Oldani, E. Marceca, M. Fujii, S.-I. Ishiuchi, M. Miyazaki, M. Broquier, C. Dedonder and C. Jouvet, *J. Chem. Phys.*, 2010, **133**, 124313.
50 H. An and K. K. Baeck, *J. Phys. Chem. A*, 2011, **115**, 13309.
51 R. N. Dixon, T. A. A. Oliver and M. N. R. Ashfold, *J. Chem. Phys.*, 2011, **134**, 194303.
52 Y. Zhang, T. A. A. Oliver, M. N. R. Ashfold and S. E. Bradforth, *Faraday Discuss.*, 2012, **157**, 141.
53 G. M. Roberts, A. S. Chatterly, J. D. Young and V. G. Stavros, *J. Phys. Chem. Lett.*, 2012, **3**, 348.
54 S. G. Ramesh and W. Domcke, *Faraday Discuss.*, 2013, **163**, 73.
55 X. Zhu and D. R. Yarkony, *J. Chem. Phys.*, 2014, **140**, 024112.
56 M. C. Capello, M. Broquier, S.-I. Ishiuchi, W. Y. Sohn, M. Fujii, C. Dedonder-Lardeux, C. Jouvet and G. A. Pino, *J. Phys. Chem. A*, 2014, **118**, 2056.

57 T. N. V. Karsili, A. M. Wenge, B. Marchetti and M. N. R. Ashfold, *Phys. Chem. Chem. Phys.*, 2014, **16**, 588.
58 B. J. Braams and J. M. Bowman, *Int. Rev. Phys. Chem.*, 2009, **28**, 577.
59 J. M. Bowman, B. J. Braams, S. Carter, C. Chen, G. Czakó, B. Fu, X. Huang, E. Kamarchik, A. R. Sharma, B. C. Shepler, Y. Wang and Z. Xie, *J. Phys. Chem. Lett.*, 2010, **1**, 1866.
60 Y. Paukku, K. R. Yang, Z. Varga and D. G. Truhlar, *J. Chem. Phys.*, 2013, **139**, 044309.
61 R. Dawes, D. L. Thompson, Y. Guo, A. F. Wagner and M. Minkoff, *J. Chem. Phys.*, 2007, **126**, 184108.
62 Y. Guo, I. Tokmakov, D. L. Thompson, A. F. Wagner and M. Minkoff, *J. Chem. Phys.*, 2007, **127**, 214106.
63 J. D. Bender, S. Doraiswamy, D. G. Truhlar and G. Candler, *J. Chem. Phys.*, 2014, **140**, 054302.
64 K. R. Yang, X. Xu and D. G. Truhlar, *J. Chem. Theory Comput.*, 2014, **10**, 924.
65 B. Wang, K. R. Yang, X. Xu, M. Isegawa, H. R. Leverentz and D. G. Truhlar, *Acc. Chem. Res.*, DOI: 10.1021/ar500068a, online as Article ASAP.
66 S. Dasgupta and W. A. Goddard III, *J. Chem. Phys.*, 1989, **90**, 7207.
67 V. Barone, I. Cacelli, N. De Mitri, D. Licari, S. Monti and G. Prampolini, *Phys. Chem. Chem. Phys.*, 2013, **15**, 3736.
68 H. Nakano, *J. Chem. Phys.*, 1993, **99**, 7983; H. Nakano, *Chem. Phys. Lett.*, 1993, **207**, 372.
69 E. Papajak and D. G. Truhlar, *J. Chem. Theory Comput.*, 2011, **7**, 10.
70 P. Siegbahn, A. Heiberg, B. O. Roos and B. A. Levy, *Phys. Scr.*, 1980, **21**, 323; B. O. Roos, P. R. Taylor and P. E. M. Siegbahn, *Chem. Phys.*, 1980, **48**, 157; K. Ruedenberg, M. W. Schmidt, G. M. Gilbert and S. T. Elbert, *Chem. Phys.*, 1982, **71**, 41.
71 T. H. Dunning, Jr, *J. Chem. Phys.*, 1989, **90**, 1007; R. A. Kendall and T. H. Dunning, Jr, *J. Chem. Phys.*, 1992, **96**, 6796.
72 Y. P. Varshni, *Rev. Mod. Phys.*, 1957, **29**, 664, erratum: 1959, **31**, 839.
73 P. M. Morse, *Phys. Rev.*, 1929, **34**, 1957.
74 Y. Zhao and D. G. Truhlar, *Theor. Chem. Acc.*, 2008, **120**, 215.
75 M. E. Casida, C. Jamorski, K. C. Casida and D. R. Salahub, *J. Chem. Phys.*, 1998, **108**, 4439.
76 R. E. Stratmann, G. E. Scuseria and M. J. Frisch, *J. Chem. Phys.*, 1998, **109**, 8218.
77 G. Simons, R. G. Parr and J. M. Finlan, *J. Chem. Phys.*, 1973, **84**, 891.
78 S. Gupta, K. Dharamvir and V. K. Jindal, *Int. J. Mod. Phys. B*, 2004, **18**, 1021.
79 G. Pongor, G. Fogarasi, J. E. Boggs and P. Pulay, *J. Mol. Spectrosc.*, 1985, **114**, 445.
80 See ESI† at [URL will be inserted by RSC] for additional details of the fitting of the potential energy surfaces and the full set of final parameters.
81 R. J. Duchovic, Y. L. Volobuev, G. C. Lynch, T. C. Allison, J. C. Corchado, D. G. Truhlar, A. F. Wagner and B. C. Garrett, *Comput. Phys. Commun.*, 2002, **144**, 169–187, erratum: 2004, 156, 319–322.
82 See http://comp.chem.umn.edu/potlib/for the latest version of POTLIB that includes the phenol potential energy surface matrix presented in this paper.
83 H. Nakamura, J. D. Xidos, A. C. Chamberlin, C. P. Kelly, R. Valero, K. R. Yang, J. D. Thompson, J. Li, G. D. Hawkins, T. Zhu, B. J. Lynch, Y. Volobuev, D. Rinaldi, D. A. Liotard, C. J. Cramer and D. G. Truhlar, HONDOPLUS-v5.2, University of Minnesota, Minneapolis, MN, 2013.
84 M. J. Frisch, G. W. Trucks, H. B. Schlegel, G. E. Scuseria, M. A. Robb, J. R. Cheeseman, G. Scalmani, V. Barone, B. Mennucci, G. A. Petersson, H. Nakatsuji, M. Caricato, X. Li, H. P. Hratchian, A. F. Izmaylov, J. Bloino, G. Zheng, J. L. Sonnenberg, M. Hada, M. Ehara, K. Toyota, R. Fukuda, J. Hasegawa, M. Ishida, T. Nakajima, Y. Honda, O. Kitao, H. Nakai, T. Vreven, J. A. Montgomery, Jr J. E. Peralta, F. Ogliaro, M. Bearpark, J. J. Heyd, E. Brothers, K. N. Kudin, V. N. Staroverov, R. Kobayashi, J. Normand, K. Raghavachari, A. Rendell, J. C. Burant, S. S. Iyengar, J. Tomasi, M. Cossi, N. Rega, J. M. Millam, M. Klene, J. E. Knox, J. B. Cross, V. Bakken, C. Adamo, J. Jaramillo, R. Gomperts, R. E. Stratmann, O. Yazyev, A. J. Austin, R. Cammi, C. Pomelli, J. W. Ochterski, R. L. Martin, K. Morokuma, V. G. Zakrzewski, G. A. Voth, P. Salvador, J. J. Dannenberg, S. Dapprich, A. D. Daniels, Ö. Farkas, J. B. Foresman, J. V. Ortiz, J. Cioslowski and D. J. Fox, *Gaussian 09, Revision D.01*, Gaussian, Inc., Wallingford CT, 2009.
85 J. Zheng, S. Zhang, B. J. Lynch, J. C. Corchado, Y.-Y. Chuang, P. L. Fast, W.-P. Hu, Y.-P. Liu, G. C. Lynch, K. A. Nguyen, C. F. Jackels, A. Fernandez Ramos, B. A. Ellingson, V. S. Melissas, J. Villà, I. Rossi, E. L. Coitiño, J. Pu, T. V. Albu, R. Steckler, B. C. Garrett, A. D. Isaacson and D. G. Truhlar, POLYRATE–version 2010, University of Minnesota, Minneapolis, 2010.
86 J. Zheng, Z. H. Li, A. W. Jasper, D. A. Bonhommeau, R. Valero, R. Meana-Pañeda and D. G. Truhlar, ANT–version 2014, University of Minnesota, Minneapolis, MN, 2014, http://comp.chem.umn.edu/ant, accessed May 26 2014.
87 N. W. Larsen, *J. Mol. Struct.*, 1979, **51**, 175.
88 G. Portalone, G. Schultz, A. Domenicano and I. Hargittai, *Chem. Phys. Lett.*, 1992, **197**, 482.
89 D. Spangenberg, P. Imhof and K. Kleinermanns, *Phys. Chem. Chem. Phys.*, 2003, **5**, 2505.
90 C.-W. Cheng, Y.-P. Lee and H. A. Witek, *J. Phys. Chem. A*, 2008, **112**, 2648.
91 F. van Bolhuis and C. T. Kiers, *Acta Crystallogr., Sect. B: Struct. Crystallogr. Cryst. Chem.*, 1978, **34**, 1015.
92 G. Keresztury, F. Billes, M. Kubinyi and T. Sundius, *J. Phys. Chem. A*, 1998, **102**, 1371.
93 J. Spanget-Larsen, M. Gil, A. Gorski, D. M. Blake, J. Waluk and J. G. Radziszewski, *J. Am. Chem. Soc.*, 2003, **123**, 11253.

94 I. M. Alecu, J. Zheng, Y. Zhao and D. G. Truhlar, *J. Chem. Theory Comput.*, 2010, **6**, 2872.
95 R. C. Fuh, Oregon Medical Laser Center, Portland, OR, 1995, http://omlc.ogi.edu/spectra/PhotochemCAD/html/072.html, accessed May 17 2014.
96 R. F. Gunion, M. K. Gilles, M. L. Polak and W. C. Lineberger, *Int. J. Mass Spectrom. Ion Processes*, 1992, **117**, 602.
97 J. G. Radziszewski, M. Gil, A. Gorski, J. Spanger-Larsen, J. Waluk and B. J. Mróz, *J. Chem. Phys.*, 2001, **115**, 9733.
98 Y.-R. Luo, *Handbook of Bond Dissociation Energies in Organic Compounds*, University of Science and Technology of China, Hefei, 2006, p. 182.
99 H. D. Bist, J. C. D. Brand and D. R. Williams, *J. Mol. Spectrosc.*, 1966, **21**, 76; H. D. Bist, J. C. D. Brand and D. R. Williams, *J. Mol. Spectrosc.*, 1967, **24**, 402; H. D. Bist, J. C. D. Brand and D. R. Williams, *J. Mol. Spectrosc.*, 1967, **24**, 413.
100 O. Tishchenko, D. G. Truhlar, A. Ceulemans and M. T. Nguyen, *J. Am. Chem. Soc.*, 2008, **130**, 7000.
101 D. G. Truhlar and A. Kuppermann, *J. Am. Chem. Soc.*, 1971, **93**, 1840.
102 A. D. Isaacson and D. G. Truhlar, *J. Chem. Phys.*, 1981, **75**, 4090.
103 M. Page and J. W. McIver, Jr, *J. Chem. Phys.*, 1988, **88**, 922.
104 J. O. Hirschfelder and E. Wigner, *J. Chem. Phys.*, 1939, **7**, 616.
105 M. A. Eliason and J. O. Hirschfelder, *J. Chem. Phys.*, 1959, **30**, 1426.
106 R. A. Marcus, *J. Chem. Phys.*, 1967, **46**, 959.
107 R. T. Skodje, D. G. Truhlar and B. C. Garrett, *J. Chem. Phys.*, 1982, **77**, 5955.
108 Y.-P. Liu, G. C. Lynch, T. N. Truong, D.-h. Lu, D. G. Truhlar and B. C. Garrett, *J. Am. Chem. Soc.*, 1993, **115**, 2408.
109 D. C. Chatfield, R. S. Friedman, D. G. Truhlar, B. C. Garrett and D. W. Schwenke, *J. Am. Chem. Soc.*, 1991, **113**, 486.
110 A. Tachibana and K. Fukui, *Theor. Chem. Acta*, 1979, **51**, 189.
111 G. C. Hancock, P. Rejto, R. Steckler, F. B. Brown, D. W. Schwenke and D. G. Truhlar, *J. Chem. Phys.*, 1986, **85**, 4997.
112 D. G. Truhlar, A. D. Isaacson, R. T. Skodje and B. C. Garrett, *J. Phys. Chem.*, 1982, **86**, 2252.
113 D. G. Truhlar, A. D. Isaacson and B. C. Garrett, in *The Theory of Chemical Reaction Dynamics*, ed. M. Baer, CRC Press, Boca Raton FL, 1985, vol. 4, pp. 65–137.
114 A. Fernandez-Ramos, B. A. Ellingson, B. C. Garrett and D. G. Truhlar, *Rev. Comput. Chem.*, 2007, **23**, 125.
115 B. C. Garrett, D. G. Truhlar, A. F. Wagner and T. H. Dunning, Jr, *J. Chem. Phys.*, 1983, **78**, 4400.
116 A. Fernandez-Ramos and D. G. Truhlar, *J. Chem. Phys.*, 2001, **114**, 1491.
117 Y.-P. Liu, D.-h. Lu, A. Gonzàlez-Lafont, D. G. Truhlar and B. C. Garrett, *J. Am. Chem. Soc.*, 1993, **115**, 7806.
118 B. C. Garrett and D. G. Truhlar, *J. Chem. Phys.*, 1983, **79**, 4931.
119 R. Meana-Pañeda, D. G. Truhlar and A. Fernández-Ramos, *J. Chem. Theory Comput.*, 2010, **6**, 6.
120 J. G. Lauderdale and D. G. Truhlar, *Surf. Sci.*, 1985, **164**, 558.
121 S. E. Wonchoba, W.-P. Hu and D. G. Truhlar, in *Theoretical and Computational Approaches to Interface Phenomena*, ed. H. L. Sellers and J. T. Golab, Plenum, New York, 1994, p. 7.
122 A. J. C. Varandas, F. B. Brown, C. A. Mead, D. G. Truhlar and N. C. Blais, *J. Chem. Phys.*, 1987, **86**, 6258.
123 E. B. Wilson, *Phys. Rev.*, 1934, **45**, 706.
124 Y. Zhao and D. G. Truhlar, *J. Chem. Phys.*, 2006, **125**, 194101.
125 H.-D. Meyer and W. H. Miller, *J. Chem. Phys.*, 1979, **70**, 1334.
126 A. D. Micha, *J. Chem. Phys.*, 1983, **78**, 7138.
127 M. Amarouche, F. X. Gadea and J. Durup, *Chem. Phys.*, 1989, **130**, 145.
128 M. D. Hack and D. G. Truhlar, *J. Chem. Phys.*, 2001, **114**, 9305.
129 M. J. Bearpark, M. A. Robb and H. B. Schlegel, *Chem. Phys. Lett.*, 1994, **223**, 269.
130 M. Dallos, H. Lischka, R. Shepard, D. R. Yarkony and P. G. Szalay, *J. Chem. Phys.*, 2004, **120**, 7330.
131 S. Nangia and D. G. Truhlar, *J. Chem. Phys.*, 2006, **124**, 124309.
132 Z. H. Li, R. Valero and D. G. Truhlar, *Theor. Chem. Acc.*, 2007, **118**, 9.

